THESIS FOR THE DEGREE OF DOCTOR OF PHILOSOPHY

First principles study of tungsten-based alloys: From defect thermodynamics to phase diagrams

LEILI GHARAEE

Department of Physics
Chalmers University of Technology
Göteborg, Sweden 2017

First principles study of tungsten-based alloys:
From defect thermodynamics to phase diagrams
LEILI GHARAEE
ISBN 978-91-7597-571-9

Doktorsavhandlingar vid Chalmers tekniska högskola
Ny serie nr 4252
ISSN 0346-718X

Department of Physics
Chalmers University of Technology
SE-412 96 Göteborg, Sweden
Telephone +46 31 772 8417

Cover: Schematic illustration of a binary alloy phase diagram. The heat map represents the temperature change, and the configurations on the x-axis demonstrate different alloy compositions.

Typeset in XƎLaTeX with Linux Libertine and Sans Serif. Figures created using Gnuplot, OVITO [1], Inkscape, and Blender.

Chalmers reproservice
Göteborg, Sweden 2017

First principles study of tungsten-based alloys:
From defect thermodynamics to phase diagrams

LEILI GHARAEE
Department of Physics
Chalmers University of Technology

Abstract

Nuclear fusion is a very attractive option for energy production as it is clean, safe and efficient. The major obstacle in construction of fusion power plants is the development of materials that can tolerate the extreme operational condition especially high-energy neutron flux. Tungsten is the prime candidate as armor material in fusion reactors due to its high strength and excellent high temperature properties. Tungsten alloys are interesting in this context because of the transmutation of tungsten to other elements upon neutron irradiation. In this thesis, properties of tungsten alloys were studied by means of first-principles calculations based on density functional theory (DFT). I investigated the thermodynamic and kinetic properties of intrinsic and extrinsic defects in tungsten. Ti, V and Re were shown to trap self-interstitials. Whereas mixed-interstitial migration was found to proceed via a non-dissociative mechanism with a lower barrier than that of vacancies.

A closer look at trapping effects in W-Re, W-V, and W-Ti alloys showed that mixed-interstitials in all systems are strongly attracted to each other with large binding energies. They form interstitial pairs aligned along parallel first-neighbor $\langle 111 \rangle$ strings. This behavior is caused by the very large and anisotropic strain field of these interstitial defects. Low barriers for defect translation and rotation enable defect agglomeration and alignment even at moderate temperatures. Re-rich clusters that are observed in irradiated tungsten, at concentrations below the solubility limit, may eventually transform into intermetallic phases, which can affect materials hardness and embrittlement. To explain the formation of these precipitates, I carried out DFT calculations to characterize the landscape for diffusion. My results were subsequently used by collaborators to parametrize a kinetic Monte Carlo model. Simulations based on this model showed that both vacancy and interstitial mediated transports control cluster nucleation. Re-rich precipitates were seen to grow by attracting more mixed interstitials bringing solute atoms, which in turn attracted vacancies leading to recombination and solute agglomeration.

The heat of mixing for the previously mentioned alloying elements was investigated further. For W-Ti, the equilibrium phase diagram below 1700 K is not known due to experimental difficulties. The present study revealed a negative heat of formation on the W-rich side, which is consistent with the experimentally observed asymmetric solubility. A revised solubility limit at low temperatures of the W-Ti phase diagram was derived on the basis of these calculations.

Finally I assessed the performance of constraint-based functionals and considered the recently-developed consistent-exchange van der Waals density functional version vdW-DF-cx, the semi-local PBE and PBEsol functionals as well as the AM05 meta-functional. Structural and thermophysical properties of 3d, 4d, and 5d non-magnetic transition metals were computed at finite temperatures. It was shown that overall vdW-DF-cx provides an accurate description of thermophysical properties that is typically superior to the other functionals considered. It can thus be used to study systems that have both sparse and dense electron distributions .

Keywords: tungsten alloys, point defects, irradiation, structural materials, first-principles calculations.

LIST OF PUBLICATIONS

This thesis consists of an introductory text and the following papers:

I **A first-principles investigation of interstitial defects in dilute tungsten alloys**
Leili Gharaee and Paul Erhart
Journal of Nuclear Materials **467**, 448-456 (2015).

II **The role of interstitial binding in radiation induced segregation in W-Re alloys**
Leili Gharaee, Jaime Marian and Paul Erhart
Journal of Applied Physics **120**, 025901 (2016).

III **Mechanism of Re precipitation in irradiated W-Re alloys from kinetic Monte Carlo simulations**
Chen-Hsi Huang, Leili Gharaee, Yue Zhao, Paul Erhart and Jaime Marian
arXiv preprint arXiv:1702.03019 (2017).

IV **Finite-temperature properties of non-magnetic transition metals: Comparison of the performance of constraint-based semi and nonlocal functionals**
Leili Gharaee, Paul Erhart and Per Hyldgaard
Physical Review B **95**, 085147 (2017)

V **Structurally driven asymmetric miscibility in the phase diagram of W-Ti**
Leili Gharaee, Mattias Ångqvist, Magnus Rahm and Paul Erhart
(In manuscript)

The author's contribution to the papers:

I The author carried out the calculations, analysis, and wrote most of the paper.

II The author carried out the calculations, analysis, and wrote most of the paper.

III The author carried out the DFT and NEB calculations and assisted in writing the paper.

IV The author did most of the calculations and assisted in writing the paper.

V The author carried out the DFT calculations, extracted the free energies, constructed the phase diagram and wrote the first draft of the paper.

Contents

1

Introduction

The world energy demand grows rapidly as the global population expands, countries grow economically, and people desire higher standards of living. In this regard, nuclear fusion is expected to play a key role because it is a clean and sustainable source of energy. Fusion offers important advantages such as no carbon emissions and therefore no air pollution, unlimited fuel supply and intrinsically safe technology, which would make a massive contribution to mitigating concerns about energy safety and climate change.

Currently, three main projects, JET (Joint European Torus), ITER (International Thermonuclear Experimental Reactor), and DEMO (DEMOnstration Power Plant), are hoping to pave the way for commercially viable power generation using nuclear fusion.

JET, located in Oxfordshire, UK, set the world record in 1997, for achieving (16 MW) fusion power in deuterium-tritium operation [2], the fuel proposed for the first generation of fusion power plants. The follow-up programme, ITER, will attempt to go one step further and generate more power, 500–700 MW [3], than is used to start the process. This project attempts to demonstrate the feasibility of magnetic-confinement nuclear fusion and is currently under construction in Cadarache, France.

ITER, however, does not represent the final step; It is the bridge toward DEMO, the first plant that will demonstrate large-scale production of electrical power and tritium fuel self-sufficiency. Planning for DEMO design and operation is still ongoing as it depends also on the results of the early years of operation in ITER. Conceptual designs of DEMO sketch a machine that is larger than ITER with the ability to produce fusion power output in range of 30 to 50 times larger than the input power. The size of the machine is determined by the radius of the plasma cross-section, which is confined in a doughnut-shaped vessel. Its radius for DEMO ranges from 6 to 10 metres. In comparison, the radius in ITER measures 6.2 meters and that of the largest tokamak in operation, JET, measures about half of that [2, 3, 4, 5].

One of the main concerns during reactor operation is the severe radiation conditions expected in fusion reactors, which requires the development of new materials able to withstand the harsh environment including thermal loads and radiation. The high-energy and high-intensity neu-

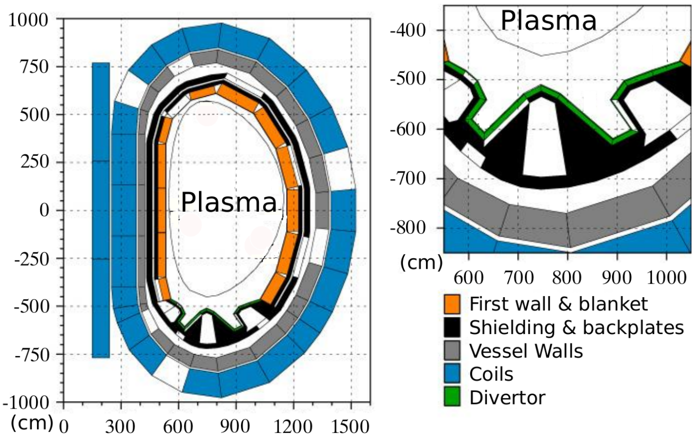

Figure 1.1: A toroidal section through a simplified DEMO model. (Source of image: Ref. [6])

tron fluxes produced by the fusion plasma have a significant lifetime-limiting impact on fusion reactor components via altering mechanical and thermophysical properties.

The fusion reaction takes place in the reactor chamber inside a vacuum vessel. The vacuum vessel is the container, which houses the fusion reaction and acts as a first safety containment barrier. At the very bottom of the vacuum vessel, the divertor is located as the next plasma-facing component, see Fig. 1.1, and its function is to extract heat and helium ash –both products of the fusion reaction– and other impurities from the plasma.

The average neutron fluence on the first wall material in ITER is 0.57-0.8 MWa/m^2 and the neutron flux at the first wall will reach up to $\sim 10^{23}$ n/m^{2}s. The average neutron fluence for DEMO is expected to be up to 15 MWa/m^2 with neutron fluxes being at least a hundred times larger. The plasma current varies from 4.8 MA in JET to 15-17 MA in ITER and 30 MA in DEMO. As a result, higher heat flux and higher neutron loads in DEMO, will lead to higher displacements per atom (dpa) of up to ~ 30 dpa, compared to ITER with < 3 dpa in a full operational life [3, 4, 5, 7, 8, 9, 10, 11].

More energetic fusion neutrons in higher doses cause far more damage and transmutation products. Transmutation in turn, results in a change in material composition and will thus influence thermal, chemical, and mechanical properties of the wall materials, which eventually has a great influence on the resistance to radiation.

While for JET, initially carbon tiles were used to cover the interior wall of the vacuum vessel, they were recently replaced with beryllium and tungsten tiles. In ITER, beryllium has been chosen to cover the first wall, while interior surfaces of the vacuum vessel will be made of high-strength copper and stainless steel.

Since the size of the vacuum vessel dictates the volume of the fusion plasma, DEMO will produce a greater amount of power and higher radiation load compared to ITER and therefore stronger materials are required. In this regard tungsten is considered for structural applications in fusion reactors due to its superior high temperature properties. Plasma-facing components of the divertor, which withstand the highest surface heat loads in ITER, are being made of tungsten [3, 4, 5, 7].

Tungsten has a high melting point, low coefficient of thermal expansion, high thermal conductivity, and excellent resistance to physical sputtering. This combination of properties makes tungsten an attractive choice as a coating material on the high heat flux components.

Yet, tungsten generally exhibits ductile behavior at high temperatures and brittle behavior at low temperatures. The ductile operating window for tungsten is about 700-1200 °C, and tungsten exhibits brittle behavior at temperatures lower than about 300 °C. Its ductile to brittle transition temperature (DBTT) lies between 150 °C and 400 °C [9]. The DBTT for tungsten is known to be relatively high, however its exact range is very much dependent on the details of the manufacturing process and the history of the material. The operational temperature for plasma facing components at the ITER divertor ranges from ∼200 °C at water cooled operation to 3000 °C at full operation, which also include the temperature range that tungsten shows brittle behavior. To solve this problem, alloying, for example by Re, has been suggested as a means to lower temperature range in which, the fracture mode of pure tungsten changes from ductile to brittle [4, 9, 11, 12, 13, 14, 15].

Alloy formation will also occur naturally due to nuclear transmutation caused by high energy neutron exposure. In this fashion, pure tungsten will gradually evolve into an W-Re-Os-Ta alloy [6, 16, 17]. As an example, the variation in concentrations of He, Re and Ta, produced in pure tungsten under neutron irradiation as a function of position in the divertor and first wall of a DEMO design is presented in Fig. 1.2.

Alloying either intentionally or implicitly affects many properties of importance such as mechanical performance, thermal conductivity, swelling resistance and oxidation behavior under irradiation. While these properties are reasonably well understood for pure tungsten, the situation is quite different in the case of alloys, especially under irradiation conditions.

Irradiation leads to the localized production of lattice defects such as vacancies and interstitials. Whereas vacancies are relatively immobile, interstitials in pure tungsten, which are commonly referred to as self-interstitial atoms, can readily migrate allowing for efficient defect recombination, which is an important factor with respect to radiation tolerance. In an alloy an attractive interaction between solute atoms and interstitials can lead to trapping of intrinsic defects, increasing the defect density after bombardment and thus accelerating damage buildup. Thus, while alloying might improve mechanical properties it can potentially simultaneously cause a degradation of the irradiation tolerance.

Void induced swelling is another challenge for tungsten as a structural material. Swelling causes dimensional changes and variations in materials properties resulting in serious problems for the reactor design. The swelling of tungsten is shown to be strongly reduced when alloyed with rhenium [18].

In addition, specific developments are aimed at suppressing the production of volatile tungsten oxide in case of a loss-of-coolant accident with air ingress so as to reduce the risk of releasing radioactive material. One proposed solution is to add small amounts of silicon and chromium to tungsten, which leads to a glassy protection layer on the tungsten surface and can reduce the tungsten oxidation rate by up to four orders of magnitude [13].

In the present thesis, I employ computational calculations to gain insight into the response

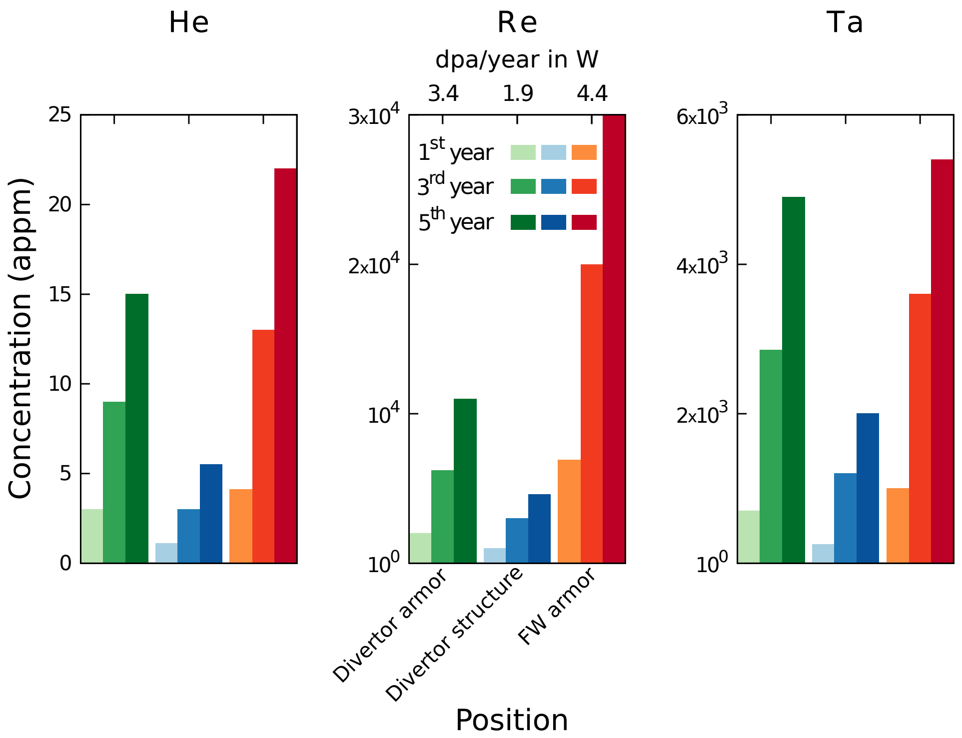

Figure 1.2: Variation in concentrations of He, Re and Ta, produced in pure tungsten under neutron irradiation as a function of position (and depth) in the divertor and first wall of the DEMO design. The equivalent dpa/year in pure tungsten are also given for each position. Units of concentrations are given in atomic parts per million (appm). (Source of data for the figure: Ref. [6])

of the material to neutron irradiation, enabling the assessment of the structural integrity of components in a fusion power plant. I provide an assessment of tungsten-based alloys for applications in fusion environments by studying different types of point defects, their interactions and diffusion as well as phase diagrams.

2

Background

2.1 Radiation and high energy particles

Irradiation is the process of exposing an object to radiation. One of the immediate effects of irradiation of a material is the displacement of some atoms from their equilibrium lattice sites. Energies vary for different radiation sources and high energy particles have a stronger impact on the material compared to the low energy ones.

Charged particles like electrons and ions, depending on their mass, interact with materials and lead to scattering. For example a 1 MeV electron in copper (Cu) can penetrate 350 μm on average, while a proton of the same energy penetrates 380 nm in Cu on average. Due to its larger mass, a proton produces more damage, loses more energy while scattering, and stops in lower depth compared to electrons. A gold (Au) ion of the same energy penetrates only 96 nm in Cu as it is heavier [19, 20].

Neutrons are not stable elementary particles and have a half-life of about 11 minutes. Free neutrons do, however, exist in situations like natural radioactive decay, which produces neutrons with energies of a few MeV. Reactions taking place in reactors produce neutrons with energies of about 2 and 14 MeV for nuclear fission and fusion respectively. Whereas neutrons do not interact significantly with electrons in the material, they interact with the atomic nuclei via the nuclear forces. Based on their energies, neutrons can interact via several different processes. While low energy neutrons interact with atoms via elastic scattering, for neutrons with energies above 1 MeV, inelastic neutron scattering becomes important. During this process, the kinetic energy is not preserved and is partially transferred into the excitation of the nucleus.

Nuclear reactions become significant for neutrons with energies above 8 MeV. During this process a nucleus absorbs the high energy neutron and generates transmutation products. This reaction is very important as it changes the composition of the material and may thereby eventually alter the properties of the material and in particular its response to irradiation [19].

2.2 Applications of high energy irradiation

High energy irradiation is an important research area with applications in various fields of technology, including diagnostic techniques and energy generation in nuclear power stations. High energy radiation is widely used in radiography for imaging the interior of objects, and in radiotherapy for medical reasons. The radiation energy varies from kilo to mega electron volts and even higher based on the type of the treatment [21, 22]. Exposure to irradiation in very large doses or for long times can be harmful and destructive for healthy tissue and therefore the dose and duration need to be selected carefully.

Another application of high energy irradiation is energy generation in nuclear power stations, where the energy of fission or fusion reactions is converted into heat and subsequently electricity. Like medical irradiation and all its other applications, irradiation in nuclear reactors has a twofold effect. On one hand, irradiation energy is converted into useful energy and on the other hand, it damages the surrounding material and degrades its properties. The issue of finding materials that can withstand high irradiation is the subject of extensive research especially for fusion reactors. In the following two subsections, a more detailed description of fission and fusion reactors is presented.

2.2.1 Nuclear fission reactor

2.2.1.1 Background

Nuclear fission is a process in which the nucleus of an atom splits. The splitting of a nucleus occurs due to radioactive decay or by bombardment by other subatomic particles. In either case, the resulting components have less combined mass compared to the original nucleus and the missing mass is converted into kinetic energy.

Radioactive fission happens primarily with the heavier elements. In this process, a nucleus of an unstable atom loses energy by emitting for instance alpha particles, beta particles, gamma rays and neutrons. Isotopes of uranium (U) by releasing hundreds of MeV energy decay to fission products such as krypton (Kr), barium (Ba), technetium (Tc), ruthenium (Ru), or palladium (Pd).

In the second mechanism, when a large fissile nucleus such as uranium-235 (^{235}U) or plutonium-239 (^{239}Pu) absorbs a neutron, it may undergo nuclear fission. The heavy nucleus splits into two or more lighter nuclei —the fission products— releasing kinetic energy, gamma radiation, and free neutrons. A portion of these neutrons may later be absorbed by other fissile atoms and trigger further fission events, which will release more neutrons. This is known as a nuclear chain reaction. This procedure releases a significant amount of energy compared to the energy of the neutron that started the procedure. Bombarding uranium with neutrons of a few eV, splits the nucleus, releasing a few hundred MeV and neutrons of ~2-3 MeV [23, 24]. Controlled reactions of this sort are used to release energy within nuclear power plants. Uncontrolled reactions can fuel nuclear weapons.

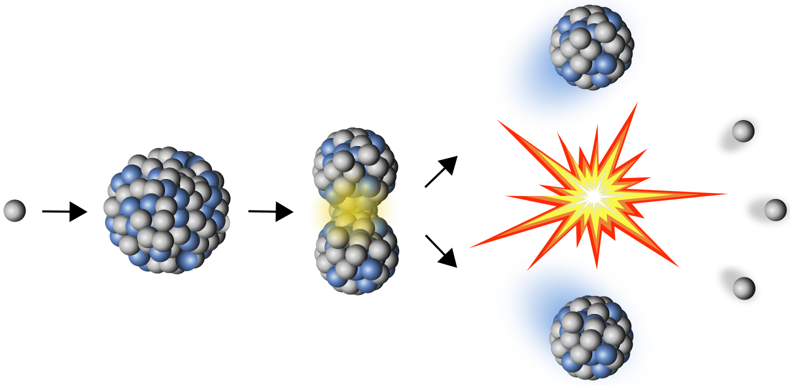

Figure 2.1: Schematic illustration of a fission process in which the nucleus of an atom breaks into smaller nuclei due to bombardment by a neutron, which results in the production of energy.

2.2.1.2 Fission reaction in nuclear reactors and electricity generation

Similar to the plants that burn coal, oil and natural gas, nuclear plants produce electricity by boiling water into steam. This steam drives turbines that produce electricity. Nuclear fuel for this process, includes two types of uranium, ^{238}U and ^{235}U, as well as plutonium. Fuel comes in the shape of solid ceramic pellets that are packaged into long tubes. ^{238}U constitutes an important share of the fuel, ^{235}U is, however, more unstable and splits quickly. This process releases neutrons, which start the chain fission reaction. Neutrons hit other uranium atoms resulting in the release of more neutrons along with heat. When a chain reaction occurs, fission becomes self-sustaining.

In order to control the nuclear reaction, special rods are inserted among the fuel tubes in order to slow down or accelerate the reaction. They are composed of chemical elements such as boron, silver, indium and cadmium that are capable of absorbing many neutrons without undergoing fission themselves [25, 26]. Fuel tubes in the reactor are surrounded by water. The heat produced during the fission reaction turns this water into steam. The steam drives turbines that power generators to create electricity.

Nuclear power provides many big advantages. It is a clean energy and does not contributes to climate change. Almost no greenhouse gases such as carbon dioxide are emitted into the atmosphere. In addition, nuclear fission has large power-generating capacity and produces roughly a million times more energy per unit weight than fossil fuel alternatives.

There are, however, negative sides to this way of energy production. Uranium sources are just as finite as other fuel sources and are expensive to mine, purify and transport. They also always possess a contamination risk. In addition, during nuclear reactor operation, a high-level radioactive waste is generated from the fuel. Lower-level radioactive waste is also generated in radiated parts and equipments, and disposal of radioactive waste is a complicated problem.

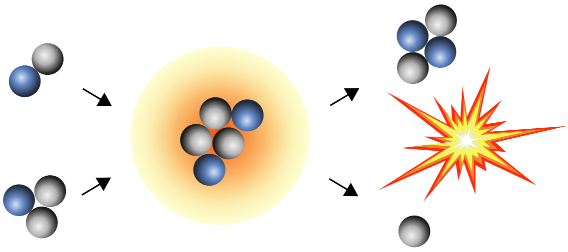

Figure 2.2: Schematic illustration of a fusion process in which deuterium and tritium fuse together, form a helium nucleus and a neutron, and release a large amount of energy.

2.2.2 Nuclear fusion reactor

With its high energy yield, low nuclear waste production, lack of air pollution and virtually limitless fuel available, fusion, the same source that powers stars, could provide an alternative to conventional energy sources.

2.2.2.1 Background

Fusion is a nuclear reaction that occurs when two or more light nuclei collide at very high speed, combine, and form a heavier atomic nucleus. A great amount of energy is released during this process in which matter is not conserved. As the total mass of the new atom is less than that of the two, from which it was formed, thus some of the matter of the fusing nuclei is converted into energy.

Fusion is the process at the core of the Sun and other stars, where hydrogen nuclei collide, fuse into heavier helium atoms and release enormous amounts of energy [27, 28]. Creating a controlled fusion reaction on Earth, however, has proven to be very difficult so far, as the two protons or hydrogen nuclei repel each other. Very specific conditions including enormous temperature and pressure are required to make it happen. The tremendous heat of the Sun, which is around ten million degrees, and its high pressure are achieved by the large mass of the Sun and the force of gravity compressing this mass in the core. This heat accelerates the atoms to the point where their momentum overcomes the Coulomb repulsion [28].

Scientists are nowadays looking for ways to control the energy produced during nuclear fusion. To this end, very high temperatures of about 100 million degrees are required, under which a hydrogen plasma is formed. Plasma is an extremely high-energy state of matter with electrons separated from the nuclei. The system is overall charge neutral yet composed of charged particles and as a result it is responsive to electromagnetic forces [28].

There are different atomic combinations, which can lead to a fusion reaction, among which, the deuterium-tritium (D-T) reaction has been identified as the most efficient combination for generating power on Earth. ITER and the future demonstration power plant DEMO, will use this combination of elements to fuel the fusion reactor [4]. In this reaction, deuterium and tritium nuclei combine to form a nucleus of Helium-4, release a neutron, and an energy of 17.6

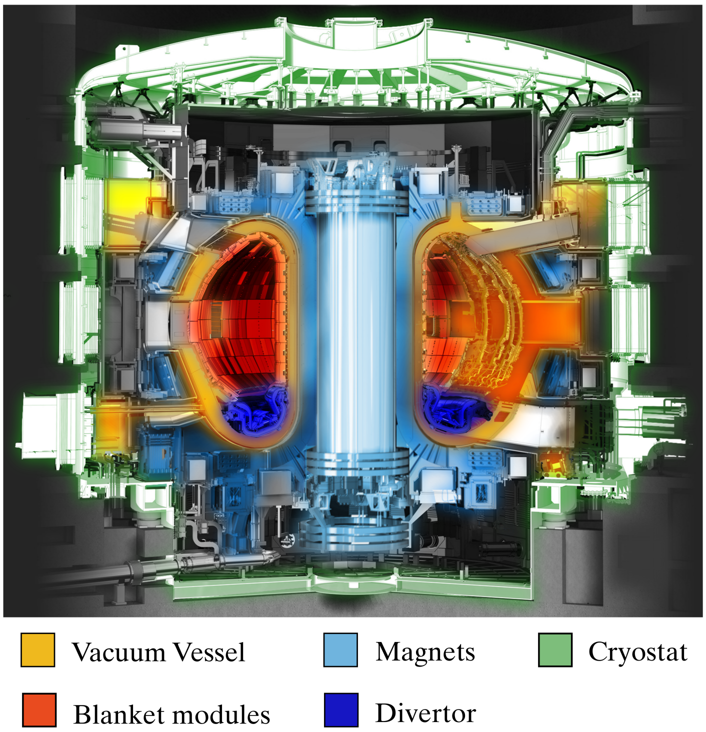

Figure 2.3: ITER tokamak reactor and its main parts including vacuum vessel, blanket modules, magnets, divertor, and the cryostat. (Source of image: Ref. [4]. The image is further customized for better illustration.)

MeV per reaction, see Fig. 2.2. Considering that billions of reactions occur in each second, one can realize the potential efficacy of the fusion reaction for generating power [28].

Deuterium is a non-radioactive isotope of hydrogen, containing a single proton and a neutron. It is widely available as it can be distilled from all forms of water. Tritium is the other isotope of hydrogen and contains one proton and two neutrons. It is a fast-decaying radioactive element, which is more challenging to locate in large quantities on Earth. Rather than attempting to find it naturally, the most reliable method is to bombard lithium with neutrons to create this element. During the fusion reaction in ITER, tritium is produced, when neutrons escaping the plasma interact with lithium contained in the blanket wall of the tokamak [4].

2.2.2.2 The working principle of a fusion reactor

In large scale commercial designs of fusion reactors, heat generated from the fusion reaction is used to operate steam turbines that drive electrical generators as in existing fossil fuel and nuclear fission power stations.

Fusion reactors are these days, however, in experimental stages and various operational concepts have been developed so far for power generation. The two main approaches to initiate nuclear fusion reactions on Earth are inertial confinement fusion and magnetic confinement fusion.

Inertial confinement is a fusion energy approach that uses high-energy laser beams to initiate the reaction by heating up and compressing a fuel target. Fuel is often provided in the form of a pellet and consists of a deuterium-tritium mixture. High energy flux laser beams are directed onto the fuel pellet, which leads to the outer layer evaporating/exploding outward. The reaction force compresses the rest of the pellet inwards. The density of the core of the pellet and subsequently its temperature rise enormously enabling it to reach the ignition point for fusion.

In the magnetic confinement approach, which is relatively more developed and well funded, neutral particle beams from accelerators are used to heat a stream of hydrogen gas and turn it into a plasma by transferring kinetic energy. This plasma is squeezed by super-conducting magnets, forcing the plasma nuclei closer to each other and thereby allowing a fusion reaction to occur. The most efficient shape for compressing the plasma is a doughnut shape or toroid in which, hot plasma is circulated in a magnetically confined ring. A reactor of this shape is called a tokamak. When completed, ITER will be the world's largest tokamak [3, 4].

The main parts of the ITER tokamak reactor, as shown in Fig 2.3, are vacuum vessel, blanket modules, magnetic field coils, cooling equipment and divertor.

The vacuum vessel is a torus-shaped double-wall structure made of steel, which houses the fusion reaction. It provides a high-quality vacuum for the plasma and serves as the first safety barrier for heat and radiation produced by the fusion reactions. Between the two walls of vacuum vessel, cooling water is circulating in order to remove the heat, which is generated during operation.

Blanket modules are located at the inner surface of the vacuum vessel and shield vacuum vessel and magnets from fusion reaction products, see Fig. 2.3. As the part which directly faces the hot plasma, neutrons reach the blanket first, slow down and loose their kinetic energy. The energy is subsequently transformed into heat and collected by the cooling water system. Eventually the heat is used to produce electricity. There are 440 blanket modules in ITER each of them measures 1×1.5 square meters and weighs up to 4.6 tonnes, see Fig. 2.3. As blanket modules face the radiation directly, the design and the choice of material for them is critical and dependent on the position in the inner surface. Beryllium for covering the first wall, and copper and stainless steel for the rest of the blanket, are the materials that have been chosen to construct blanket modules.

In ITER, magnets are placed around the vacuum vessel as well as the center in the shape of a solenoid. The function of the magnet system is to confine, shape, and control the plasma inside the vacuum vessel. It will weigh 10,000 tonnes and when completed will be the largest and most powerful magnet in the world. All ITER coils are superconducting and compared to conventional magnets carry higher current and generate a stronger magnetic field. To achieve superconductivity, magnets are cooled down using liquid helium, to temperatures of around 4 Kelvin (-269 °C). Niobium-tin (Nb_3Sn) and niobium-titanium (Nb-Ti) have been used so far to build the magnets.

The ITER cryostat is manufactured from stainless steel. It surrounds vacuum vessel and magnets and provides high vacuum and ultra-cool environment for the inner parts. With a weight of 3800 tones, the ITER cryostat is the largest vacuum chamber in the world with the

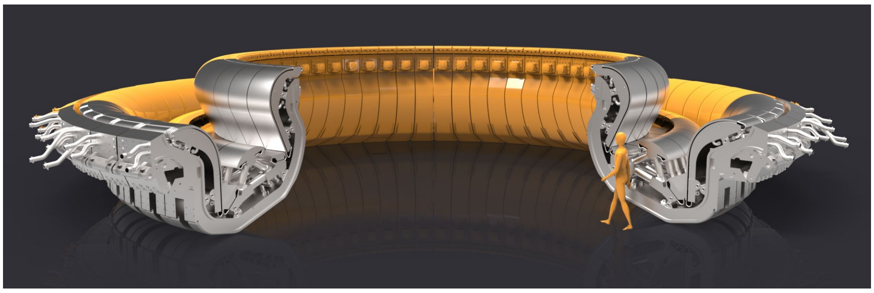

Figure 2.4: ITER divertor, which is placed at the bottom of the vacuum vessel, withstands the highest heat flux from the ITER plasma. (Source of image: Ref. [4])

ability to provide a vacuum that is 1 million times less dense than air.

Finally the divertor, situated at the bottom of the vacuum vessel, extracts waste gas and impurities from the plasma, which are generated during the fusion reaction, see Figs. 2.3 and 2.4. It comprises two main parts, a supporting structure made primarily from stainless steel, and the plasma-facing armor component, which will be made of tungsten. Tungsten has the highest melting point of all metals and it makes it a suitable choice for the plasma-facing components of the ITER divertor as it will be exposed to the highest heat load in the machine [3, 4].

In ITER, first a stream of deuterium and tritium fuel is heated to form a high-temperature plasma. In order to bring the plasma to about 150 million degrees Celsius, several heating methods will work concurrently. One source of heat is the changing magnetic field, which also controls the plasma. Magnetic fields induce a high-intensity electrical current that when it travels through the plasma, energizes electrons and ions and causes them to collide. Such collisions create resistance, which results in heat, but as the temperature of the plasma rises, this resistance —and therefore the heating effect— decreases. In order to reach higher temperatures, additional heating methods like neutral beam injection must be applied from outside the tokamak. A neutral beam injector, as an external source of heating, injects high-energy particles from the accelerator into the plasma. These neutral particles collide with plasma particles and transfer their energy to them. This helps the plasma to reach the temperature necessary for fusion.

When the fusion reaction occurs, the high energy neutrons generated during the fusion reaction will be absorbed by lithium blankets and produce more tritium fuel. This process in turn, increases the temperature of the blanket, for which cooling mechanisms are employed to decrease the temperature of the blanket by using the heat for turning water into steam and eventually producing electricity [3, 4, 29].

It has, however, been one of the big challenges to come up with a non-destructive way of performing fusion. Interior walls of the reactor are exposed to high energy neutron irradiation and high heat fluxes. High-energy fusion neutrons, when they escape the plasma, can strongly interact with the atoms of the wall material and cause structural changes via processes like atomic displacements and elemental transmutations, which may eventually lead to material degradation. It is, as a result, an essential step in fusion research to find suitable wall materials with high radiation tolerance at high temperatures.

2.3 Radiation-induced point defects

During the operation of a nuclear reactor, the immediate surrounding of the plasma is exposed to extreme neutron irradiation. When a neutron enters the wall material a collision happens and some atoms are displaced from normal lattice sites. The atomic displacement process starts with the creation of a primary knock on atom (PKA), which is any target atom struck by neutron as irradiation particle.

Neutron-atom interactions can be elastic or inelastic. Elastic interactions are important in the context of damage or defect generation as they can produce Frenkel pairs (vacancies and self-interstitials) and rearrange atoms on their lattice sites. During elastic collisions, the initial kinetic energy of PKA dissipates via two processes. The first part is lost to electronic excitations, which do not contribute to damage creation but mainly act as a viscous medium. The second dissipation channel is by elastic collisions with surrounding atoms, subsequently resulting in a cascade of collision events. Inelastic excitations, on the other hand, have a small direct effect on damage production and a significant part of the neutron energy is transferred to excite the nucleus that it strikes.

In addition to creation of the PKA, which causes displacement damage, neutron-atom interaction can lead to the transmutation. Nuclear reactions can create foreign elements or impurities, which can undergo further collisions themselves. Under high energy irradiation, the concentration of such defects increases dramatically, which affects the physical properties of the material. As this eventually changes the performance of material under irradiation, one needs to develop a detailed understanding of the structure and behavior of such defects.

2.3.1 Defects in crystalline materials

In a perfect crystal in equilibrium, all atoms are at their specific atomic sites. Real crystals and particularly materials exposed to irradiation, however, contain imperfections such as point, line, surface (planar) or volume (bulk) defects, which locally disturb the regular arrangement of the atoms.

Defects can be classified according to their dimensionality. Zero dimensional defects are called point defects and are the main focus of this work. There are two types of point defects in materials. Native defects are intrinsic to the material, such as vacancies (missing atoms) and self-interstitials (additional atoms incorporated on sites other than substitutional sites), see Fig. 2.5. In addition to intrinsic point defects, crystals may also contain extrinsic point defects, which are impurity atoms on substitutional or interstitial sites.

In addition to point defects, there are one dimensional defects, called line defects. An example of these defects are dislocations, which govern plastic deformation in many materials. Planar defects such as stacking faults and grain boundaries, are two dimensional defects. Volume or bulk defects are three dimensional crystal defects. Precipitates, voids and bubbles belong to this category of defects [30].

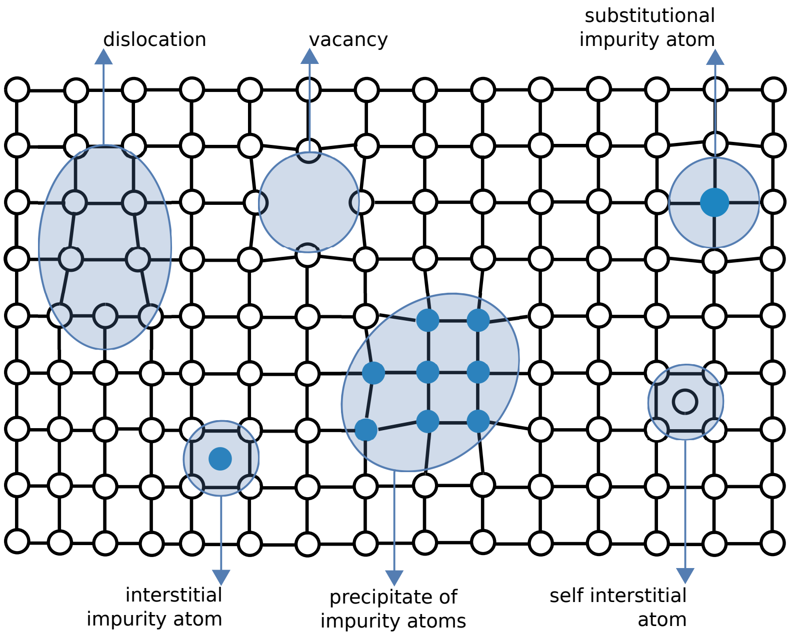

Figure 2.5: Schematic illustration of a number of crystallographic defects.

2.4 Tungsten as a first wall material

Plasma-wall interaction issues are among the most serious obstacles to the realization of fusion energy production. This interaction is a key factor, which determines the safety and lifetime of the wall components and subsequently the overall cost-effectiveness of the facility.

The structural materials have to meet a vast numbers of criteria to be safe, suitable and efficient for a fusion environment. For example they have to show low erosion, which favors heavy elements such as Mo or W. It is also required for these materials to have high melting point and high thermal conductivity, for which the candidate materials are C and W. With regard to low radiation loss and low nuclear activation lighter elements such as Be and C are good candidates. Low propensity to absorb tritium is also very important; W and —to a lesser extent— steel and beryllium meet this criterion.

Tungsten and tungsten alloys are therefore considered for structural applications in fusion reactors, especially for armor materials at the divertor and first wall [11, 31, 32, 33]. In ITER, tungsten is suggested for plasma-facing armor components of the divertor as the region with highest heat load, see Fig. 2.3 and 2.4 and to this end, the behavior of these materials under irradiation has to be investigated carefully.

2.4.1 Behavior under irradiation

During fusion reactor operation, as a result of high energy neutron exposure, displacement damage occurs and several defects are formed and interact. Nuclear transmutation happens as well, and results in compositional changes and additional defect interactions. Tungsten is also exposed to hydrogen and helium particles arriving at its surface from the plasma.

Vacancies and interstitials are among the point defects generated under irradiation. Whereas vacancies are relatively immobile, interstitials in pure tungsten can readily migrate, allowing for efficient defect recombination, which is an important factor with respect to radiation tolerance [34, 35, 36]. In an alloy, an attractive interaction between solute atoms and interstitials can lead to trapping of defects, increasing the defect density compared to the pure material. Thus alloying can potentially cause a degradation of the irradiation tolerance.

Tungsten transmutes to rhenium, osmium and tantalum in a fusion neutron environment. At the first wall armor of a nuclear fusion device, it has been estimated that after five years of operation, pure tungsten transmutes into an alloy containing Re and Ta with concentration of 3% Re and 0.6% Ta [6], see Fig. 1.2. Another study predicted that W transmutes to an end-of-service alloy composition of approximately 91 at% W, 6 at% Re and 3 at% Os at the first wall armor [37]. The amount of He produced in the divertor armor was found to be negligible compared to other transmuted elements. After a five-year full-power irradiation the He concentration was found to be about 20 appm (0.0020%) or less depending on position [6, 37]. The amount of transmuted elements in armor tungsten varies with the magnitude of the neutron flux and the position in the first wall.

In addition to neutrons, tungsten is also exposed to hydrogen particles. Under continuous high-flux radiation at moderate temperatures (<800 K) blistering occurs for tungsten surfaces. The hydrogen concentration can locally increase and exceed the solubility limit of the tungsten, which may be the cause of blistering [38, 39].

Blistering also occurs by helium bombardment. Formation of holes and bubbles by helium at higher temperatures (>1600 K) is a drawback of tungsten under irradiation conditions. The formation of these defects has been attributed to the accumulation of helium in defects and vacancy sites. The size of such nanostructures is found to be dependent on the surface and exposure temperature, and the incident ion energy [39, 40, 41, 42].

Finally tungsten exhibits brittle behavior at low temperatures and ductile behavior at high temperatures. The brittle-to-ductile transition temperature (BDTT) of pure tungsten is high, which poses a challenge with respect to its applications in fusion environment [11, 14, 43]. It has been found that the ductility of tungsten can be improved by alloying with rhenium, which is also a transmutational element in tungsten [16, 44, 45]. On the other hand, Re and Os are shown to precipitate under irradiation with the solute concentration below their solubility limit. Such radiation-induced precipitation (RIP) of Re is observed in W in the form of intermetallic σ and χ phases. Os is also seen to precipitate in W under irradiation and the crystal structure of the precipitate is close to the σ phase. Such incoherent precipitates can hinder dislocation motion and eventually lead to radiation hardening and embrittlement. In this sense, irradiation of W would be harmful [37].

3

Computational details and methodology

3.1 The quantum-mechanical many-body problem

In principle, most properties of a system can be derived from the quantum mechanical wave function of the system. This wave function can be obtained by solving the time independent Schrödinger equation

$$H\Psi(\boldsymbol{r}_1, \boldsymbol{r}_2, ..., \boldsymbol{R}_1, \boldsymbol{R}_2, ...) = E\Psi(\boldsymbol{r}_1, \boldsymbol{r}_2, ..., \boldsymbol{R}_1, \boldsymbol{R}_2, ...). \tag{3.1}$$

Here $\Psi(\boldsymbol{r}_1, \boldsymbol{r}_2, ..., \boldsymbol{R}_1, \boldsymbol{R}_2, ...)$ is the quantum mechanical wave function of the system and $\boldsymbol{r}_i$ and $\boldsymbol{R}_I$ denote the positions of the ith electron and the Ith nucleus. E corresponds to the ground state energy of the system.

The complete Hamiltonian operator of the system is

$$H = -\frac{1}{2}\sum_i \nabla_i^2 - \frac{1}{M_I}\sum_I \nabla_I^2 + \frac{1}{2}\sum_{i \neq j} \frac{1}{|\boldsymbol{r}_i - \boldsymbol{r}_j|} - \sum_{i,I} \frac{Z_I}{|\boldsymbol{r}_i - \boldsymbol{R}_I|} + \frac{1}{2}\sum_{I \neq \mathrm{J}} \frac{Z_I Z_\mathrm{J}}{|\boldsymbol{R}_I - \boldsymbol{R}_\mathrm{J}|}, \tag{3.2}$$

where atomic units have been used ($\hbar = m_e = e = 4\pi\epsilon_0 = 1$) and Z_I and M_I denote charge and mass of the nuclei, respectively. Equation (3.2) can be written as

$$H = T_e(\boldsymbol{r}) + T_N(\boldsymbol{R}) + V_{ee}(\boldsymbol{r}) + V_{eN}(\boldsymbol{r}, \boldsymbol{R}) + V_{NN}(\boldsymbol{R}), \tag{3.3}$$

where T_e and T_N are the kinetic energy operators for the electrons and nuclei respectively and V_{ee}, V_{eN}, and V_{NN} represent the potentials due to Coulomb interactions between electrons and nuclei.

Obtaining a direct numerical solution for the Schrödinger equation is a difficult task because any finite-size piece of material contains a number of electrons and nuclei on the order of Avogadro's constant ($N_A \sim 10^{23}$). Since the exact solution is only possible for very small systems, simplifications and approximations to this equation are required.

3.2 The Born-Oppenheimer approximation

A key point when applying quantum mechanics to atoms is that atomic nuclei are much heavier than individual electrons, which means that electrons respond much more rapidly to changes in their surrounding than the nuclei. The Born-Oppenheimer approximation takes advantage of this observation and makes the assumption that the ions are stationary and their motion can be treated classically, while solving the electronic Schrödinger equation. As a result, the physical problem is split into two parts, the electronic structure problem and the ionic problem. The wave function of the system then becomes the product of electronic and ionic wave functions, and the electronic Hamiltonian reduces to

$$H_e = T_e(\boldsymbol{r}) + V_{ee}(\boldsymbol{r}) + V_{ext}(\boldsymbol{r}, \boldsymbol{R}), \tag{3.4}$$

where T_e and V_{ee} have been introduced above, and V_{ext} is the external potential from the nuclei including the electrostatic interactions between nuclei. In this approximation, wave function and ground state energy depend parametrically on the positions of the nuclei

$$H\Psi(\{\boldsymbol{r}\}; \{\boldsymbol{R}\}) = E(\{\boldsymbol{R}\})\,\Psi(\{\boldsymbol{r}\}; \{\boldsymbol{R}\}). \tag{3.5}$$

Here, the function $E(\{\boldsymbol{R}\})$ represents the so-called Born-Oppenheimer potential energy surface, and the nuclei are considered as classical point particles, which move on the Born-Oppenheimer potential energy surface.

Despite the fact that at this point the Hamiltonian of the system became simpler, see Eq. (3.4), still a complex term remains in the formula. The second term, which represents the electron-electron interactions requires all the electrons in the system to be treated simultaneously. For the hydrogen atom it is possible to obtain an exact numerical solution to the Schrödinger equation using this Hamiltonian, but for larger systems a different approach is required.

3.3 Density functional theory

Density functional theory (DFT) was developed as a means to solve the Schrödinger equation for a large number of atoms. In quantum mechanics, the wave function for a system of N interacting electrons is a function of the positions of all electrons in the system, equivalent to $3N$ variables. In density functional theory, the problem of determining this quantum mechanical wave function is replaced by the problem of finding the electron density of the ground state. The electron density is only a function of three spatial coordinates, which simplifies the problem considerably.

3.3.1 The Hohenberg-Kohn theorems

The entire field of density functional theory rests on two fundamental theorems proved by Kohn and Hohenberg and the derivation of a set of equations by Kohn and Sham in the mid-1960s [46, 47].

The first theorem proved by Hohenberg and Kohn states that the ground state wave function is a unique functional of the ground state electron density [46]. This implies that when the ground state density is known, the ground state wave function, energy and all other ground state properties of the system can be determined.

The second theorem states the relation between energy and the ground state density. For a system with electron density $n(\boldsymbol{r})$, the energy can be expressed as a functional of the density

$$E\,[n(\mathbf{r})] = F\,[n(\boldsymbol{r})] + \int n(\boldsymbol{r})\, V_{\text{ext}}[n(\boldsymbol{r})]\, dr, \tag{3.6}$$

in which, $F[n(\boldsymbol{r})]$ contains the kinetic energy and contributions from electron-electron interactions. The minimum of the energy functional is given by the ground state density $n_0(\boldsymbol{r})$ and corresponds to the ground state energy E_0 of the system

$$E_0 = E[n_0(\boldsymbol{r})] = \min_{n(\boldsymbol{r})} E[n(\boldsymbol{r})]. \tag{3.7}$$

Thus, by minimizing the energy functional, the ground state electron density can be found. However, this is still a complex problem as the functional, which contains all effects of electron-electron interactions, is unknown.

3.3.2 The Kohn-Sham equations

In 1965 Kohn and Sham [47] presented a scheme that replaces the problem of *interacting electrons in an external potential* with the problem of *noninteracting electrons in an effective potential.* They suggested that the unknown functional $F[n(\boldsymbol{r})]$ can be divided into three terms

$$F[n(\boldsymbol{r})] = T_s[n(\boldsymbol{r})] + E_H[n(\boldsymbol{r})] + E_{xc}[n(\boldsymbol{r})], \tag{3.8}$$

where T_s is the kinetic energy of the non-interacting electrons and $E_H[n]$ is the Hartree energy given by

$$E_H[n(\boldsymbol{r})] = \int \frac{1}{2} \frac{n(\boldsymbol{r})n(\boldsymbol{r}')}{|\boldsymbol{r}-\boldsymbol{r}'|} d\boldsymbol{r} d\boldsymbol{r}'. \tag{3.9}$$

The third term, $E_{xc}[n]$, is the energy due to exchange and correlation effects. It contains many-body contributions to the kinetic energy, exchange effects related to the Pauli principle and correlation effects due to electrostatic repulsion.

By this definition, as the kinetic energy of the system of non-interacting electrons is separated, the original system can be replaced by an equivalent system of non-interacting electrons moving in an effective potential

$$V_{eff}(\boldsymbol{r}) = V_H(\boldsymbol{r}) + V_{xc}(\boldsymbol{r}) + V_{ext}(\boldsymbol{r}), \tag{3.10}$$

where the Hartree contribution is

$$V_H(\mathbf{r}) = \int \frac{n(\boldsymbol{r}')}{|\boldsymbol{r}-\boldsymbol{r}'|} d\boldsymbol{r}', \tag{3.11}$$

and the exchange-correlation potential is

$$V_{xc}(\boldsymbol{r}) = \frac{\delta E_{xc}[n(\boldsymbol{r})]}{\delta n(\boldsymbol{r})}. \tag{3.12}$$

The system of non-interacting electrons, which are coupled through the electron density, now can be described by the Kohn-Sham equations

$$\left[-\frac{1}{2}\nabla^2 + V_{eff}(\boldsymbol{r})\right] \psi_i(\boldsymbol{r}) = E_i\, \psi_i(\boldsymbol{r}), \tag{3.13}$$

where ψ_i is the single particle wave function with corresponding Kohn-Sham eigenenergy E_i. The total electron density is $n(\boldsymbol{r}) = \sum_i f_i |\psi_i(\boldsymbol{r})|^2$, where f_i is the occupation number of the one-electron state i. Since the single particle wave function is dependent on the effective potential V_{eff}, and V_{eff} is dependent on the electron density, these equations should be solved iteratively to obtain a self-consistent solution.

The ground state energy corresponding to the ground state electron density can be expressed as

$$E_0 = \sum_i f_i Ei - E_H[n_0(\boldsymbol{r})] + E_{xc}[n_0(\boldsymbol{r})] - \int n_0(\boldsymbol{r}) V_{xc}(\boldsymbol{r}) d\boldsymbol{r}. \tag{3.14}$$

At this point, by introducing the Kohn-Sham approach, the problem has been simplified significantly. However finding the exact solution is still a difficult task due to the presence of $E_{xc}[n(\boldsymbol{r})]$, which includes all the complex many-body effects of the system.

3.3.3 Exchange-correlation functionals

So far, no approximation has been made and Kohn-Sham theory is, in principle, exact. In the Kohn-Sham equation the exchange-correlation functional contains all many-body effects. The exact form of the exchange-correlation functional is, however, not known and so far many approximations have been presented with different levels of complexity. These approximations generally follow two main approaches. Functionals are either fitted to an experimental data set or constructed to satisfy physical constraints. These two approaches are also combined in the design of some functionals. In this thesis four constraint-based functionals are considered including PBE, PBESol, AM05 and vdW-DF-cx. These functionals are briefly introduced in the rest of this section.

In the local density approximation (LDA), the exchange-correlation energy depends only on the local electronic density

$$E_{\mathrm{xc}}^{\mathrm{LDA}}[n] = \int_{r} n(\boldsymbol{r})\, \epsilon_{\mathrm{xc}}^{\mathrm{LDA}}[n(\boldsymbol{r})], \tag{3.15}$$

where the exact form of $\epsilon_{\mathrm{xc}}^{\mathrm{LDA}}$ can be determined from the exact exchange-correlation energy of the homogeneous electron gas (HEG) meaning $\epsilon_{\mathrm{xc}}^{\mathrm{LDA}}[n(\boldsymbol{r})] = \epsilon_{\mathrm{xc}}^{\mathrm{HEG}}[n(\boldsymbol{r})]$.

In spite of its simplicity, the LDA is surprisingly successful in describing a wide range of materials and properties. It provides, however, only modest accuracy when it comes to systems with rapidly varying electron densities.

To reach a better accuracy in describing systems with inhomogeneous electron density, the generalized gradient approximation (GGA) was introduced. It is a collective name for approximations that use information contained in the density $n(\boldsymbol{r})$ as well as its gradient $|\nabla n(\boldsymbol{r})|$. It is often specified in terms of an enhancement factor F_{xc} of the LDA exchange

$$E_{xc}^{\mathrm{GGA}}[n] = \int_{\boldsymbol{r}} n(\boldsymbol{r})\, \epsilon_{\mathrm{x}}^{\mathrm{LDA}}(n(\boldsymbol{r}))\; F_{\mathrm{xc}}(n, |\nabla n|). \tag{3.16}$$

There are many GGA versions as there are many ways by which information from the gradient of the electron density can be included. The GGA version of Perdew, Bruke and Ernzerhof (PBE) [48], has been a particular successful general-purpose functional for systems with dense electron distributions including both individual molecules and hard materials [48, 49].

PBEsol is another constraint-based functional, which is simlar to PBE except for the gradient expansion is restored for exchange. By restoring the gradient expansion, the PBEsol functional leads to a better description of solids and their surfaces [50].

The AM05 constraint-based functional, like PBEsol, extracts the gradient-corrected correlation and performs very well at describing the structure of dense materials. It provides in principle, an exact account of exchange effects for surfaces, i.e., the boundary between regions of higher and lower electron densities, whereas for internal regions the surface-exchange description is merged with that of the LDA [51].

Several attempts have been made over the years to develop more accurate and general purpose exchange-correlation functionals. Especially the lack of van der Waals forces in the design of extensively used GGAs, necessitate the construction of new functionals with inclusion of such forces. Van der Waals forces arise from the non-local correlation between electrons. Due to their non-local nature, local or semi-local approximations cannot correctly capture these interactions. Therefore, several versions of van der Waals density functional (vdW-DF) have been developed over the years. In 2004, the van der Waals density functional for general geometries was presented, called vdW-DF or vdW-DF1 [52]. Here, the correlation in the vdW-DF method is obtained as a six-dimensional spatial integral, which non-locally depends on density

$$E_{\mathrm{c}}^{\mathrm{nl}}[n] = \frac{1}{2} \int_{\boldsymbol{r},\boldsymbol{r}'} n(\boldsymbol{r})\, \phi(\boldsymbol{r}, \boldsymbol{r}')\, n(\boldsymbol{r}'), \tag{3.17}$$

where the interaction kernel $\phi(\boldsymbol{r}, \boldsymbol{r}')$ represents the non-local coupling of the electron densities at points $\boldsymbol{r}$ and $\boldsymbol{r}'$. The full energy functional is

$$E^{\mathrm{vdW\text{-}DF}}[n] = E_0[n] + E_{\mathrm{c}}^{\mathrm{nl}}[n], \tag{3.18}$$

where E_0 contains the semi-local exchange and local correlation. In 2014, Berland and Hyldgaard [53] developed a consistent exchange (cx) part leading to the vdW-DF-cx functional that has been employed in the present work.

Calculations in papers I, II, and III included in the present thesis were obtained using the PBE functional. The performance of the PBE, PBEsol, AM05 and vdW-DF-cx functionals was compared in paper IV, and the vdW-DF-cx functional was used for the DFT calculations of paper V.

3.3.4 Plane wave basis sets and pseudopotentials

So far, by introducing the Kohn-Sham equations and the exchange-correlation functionals, we have simplified the original electronic structure problem. To find a solution to the Kohn-Sham equation, however, further considerations are required. To begin with, in practice one has to expand the wave function in a basis set. There are different basis sets available to employ. For crystalline systems it is natural to use plane wave basis sets, and to employ periodic boundary conditions due to the periodic nature of the crystal.

As a result of Bloch's theorem [54], a complete basis set is given by plane waves with wave vectors **k** within the first Brillouin zone, according to

$$\Psi_{n,\boldsymbol{k}}(\boldsymbol{r}) = \sum_{\boldsymbol{G}} c_{n,\boldsymbol{k}+\boldsymbol{G}}\, e^{i(\boldsymbol{k}+\boldsymbol{G}).\boldsymbol{r}}. \tag{3.19}$$

Here, the sum is over all reciprocal lattice vectors $\boldsymbol{G}$, and n is the index of the eigensolutions and corresponds to different bands. Since in theory there is an infinite set of $\boldsymbol{G}$ vectors, the sum is truncated in practice by choosing a cut-off energy E_{cut}, which limits the number of $\boldsymbol{G}$ vectors according to $1/2|\boldsymbol{k}+\boldsymbol{G}|^2 < E_{cut}$. For perfect crystalline systems, this approach is ideal since for representing properties of an infinite piece of material, primitive unit cells suffice.

While using a plane wave basis set simplifies the problem, the downside of this approach is that the sum converges very slowly for rapidly varying wave functions close to the nuclei. Core electrons, however, do not actively contribute to chemical bonding and as a result can be treated differently. It is therefore common to only include the valence electrons in DFT calculations. The potential of a nucleus is then replaced with an effective potential referred to as a pseudopotential, which includes the combined potential of nucleus and core electrons. The pseudopotential is constructed in a way that it produces a smooth function within the core region, which requires a lower cut off energy, while it reproduces the all-electron wave function outside the core region.

Employing pseudopotentials allows for density functional theory calculations to be performed with greater computational efficiency. Common schemes include norm-conserving pseudopotentials [55], ultrasoft pseudopotentials [56], and the projected augmented wave method (PAW) [57]. The latter has been employed for all DFT calculations in the present work.

3.4 Convergence considerations for point defects calculations

3.4.1 Size dependence

As seen in the previous section, the use of plane wave basis sets imposes periodic boundary conditions on the system. As long as the system has translational symmetry, this is not problematic.

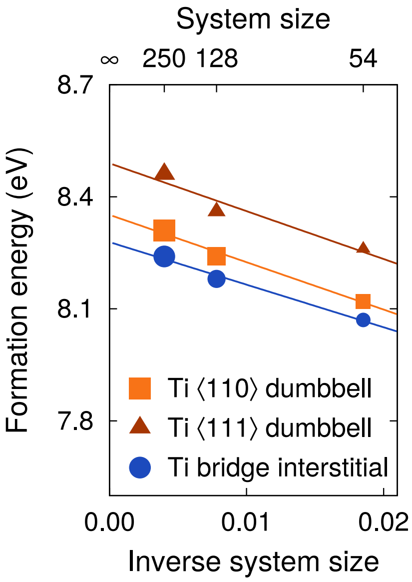

Figure 3.1: Finite size scaling of formation energies of Ti interstitial defects.

Introducing a defect into the system, however, breaks the symmetry and therefore modeling the system with periodic boundary conditions results in periodic repetition of the defects.

The most widely used methodology to describe defects in the dilute limit is the supercell approach, in which a larger cell, termed a supercell, containing the defect is constructed. If the supercell is *not* large enough, the defect will however interact with its neighboring defects because of the periodic boundary conditions, which introduces the so-called finite-size errors.

The simplest way to solve this problem is to study the convergence with respect to supercell size. When the property in question no longer changes with size, one therefore obtains the result for an isolated defect and the errors due to defect interactions are negligible. For point defects, there have been different studies in order to find a general expression for the error introduced by defect self interaction. The error has been shown to arise from two sources namely elastic and electrostatic interactions.

In the present thesis where the focus is on uncharged point defects, the dominant defect-defect interactions are elastic in nature. Elastic interactions arise from the fact that ions surrounding the defect will relax to lattice sites other than their pure equilibrium positions when the defect is introduced, resulting in lattice distortion. For a cubic supercell with size L, the elastic interaction scales with the inverse volume, L^{-3}.

In Fig. 3.1, finite size scaling of the formation energies[1] of Ti interstitial defects is presented, which clearly exhibit an inverse linear behavior with respect to volume. Relevant interstitial configurations are shown in Fig. 3.2. Smaller cells than the ones included here (e.g., a 2×2×2 16-atom cell) deviate from the inverse linear behavior because of the non-linear contributions associated with interacting defect cores.

---

[1] See Subsection 3.5.1 for the description of formation energies.

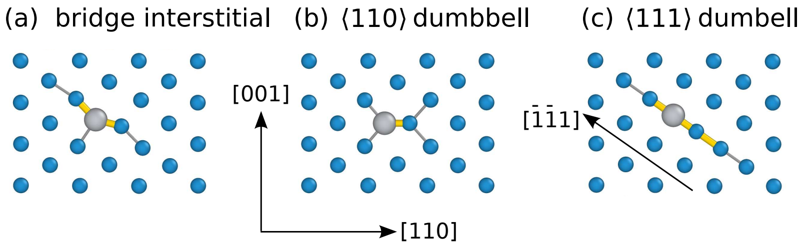

Figure 3.2: Representative configurations of (a) bridge, (b) ⟨110⟩ dumbbell, and (c) ⟨111⟩ dumbbell interstitial defects. The figure shows a slice parallel to a {110} plane of the structure. Small (blue) spheres indicate tungsten atoms whereas large (gray) spheres indicate alloying elements (like Ti) in the case of extrinsic and tungsten atoms in the case of intrinsic defects. Thicker (yellow) cylinders indicate bond lengths shorter than 2.3 Å whereas thinner (gray) cylinders indicate bond lengths shorter than 2.5 Å.

3.4.2 Brillouin zone sampling

The next source of error when calculating defects energetics using the supercell approach is related to the sampling of the Brillouin zone via a discrete $\boldsymbol{k}$-point mesh. This aspect, which is more significant in metals, results from the fact that defects in materials act as perturbations, which can cause long-range oscillations in the electronic structure (Friedel oscillations). To capture these oscillations it is not uncommon that one requires a denser $\boldsymbol{k}$-point mesh than for the corresponding defect free system.

I have studied the effect of Brillouin zone sampling for vacancies, substitutional and interstitial atoms and the results are presented in Fig. 3.3. For the tungsten vacancy one can clearly see that for a 250-atom cell (5×5×5 conventional unit cells) at least a 5×5×5 Monkhorst-Pack mesh is required in order to converge the formation energy to better than 0.1 eV. In the case of interstitials, which are also strong perturbation centers, the formation energies exhibit a slightly smaller yet still pronounced variation than for the vacancy as illustrated in Fig. 3.3 (c). Finally for substitutional defects the effect is rather weak as shown for substitutional Ti in Fig. 3.3 (b).

3.4.3 Semicore states

In the present thesis, point defects in tungsten are studied extensively. For self-interstitial atom in tungsten, it has been argued that the inclusion of semicore states, specifically W-5p states, in the pseudopotential or PAW data set is important to correctly describe the formation energies [58, 59]. This is reasonable as interstitial configurations involve very short interatomic distances and can therefore be sensitive to the core radius of the pseudopotential/PAW data set.

To quantify the effect of including semicore states, in paper I, I carried out a systematic analysis for Ti, V, Zr, Nb, Hf, Ta, and Re defects in tungsten. Our results showed that the effect of semicore states varies for different defects and elements. For instance substitutional defects are influenced negligibly with the exception of V and possibly Zr. Interstitial defects energetics are generally affected more compared to substitutionals, however, the effect ranges from almost

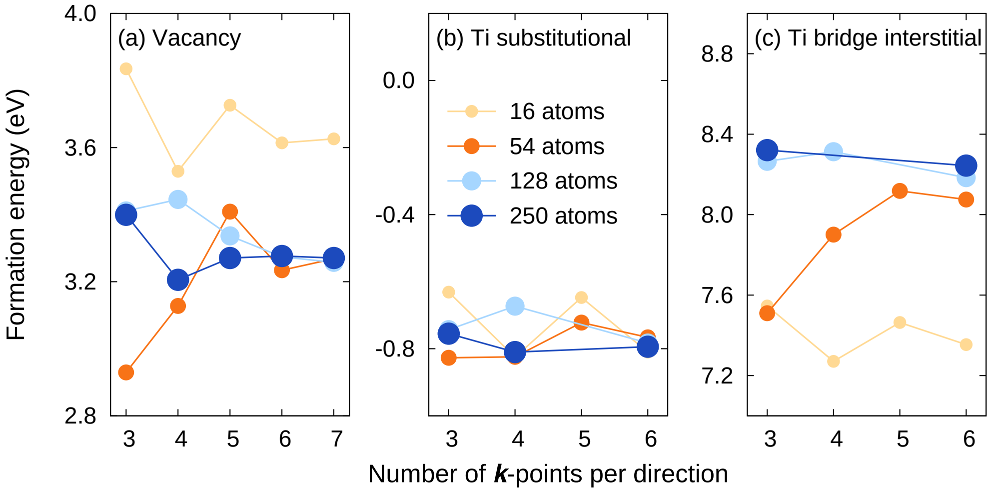

Figure 3.3: Convergence of the formation energies of (a) vacancy, (b) Ti substitutional, and (c) Ti bridge interstitial with $\boldsymbol{k}$-point density for different system sizes.

zero (Zr, Nb) to 0.5 eV and above (Ti, V, Ta). The effect of including semicore states is typically larger for $\langle 110\rangle$ interstitials, which have the shortest interatomic separation, than for $\langle 111\rangle$ and bridge interstitial configurations.

This study furthermore showed that the effect of semicore states is only weakly dependent by Brillouin zone sampling and system size. As the computational effort increases significantly due to approximately twice as many electrons in the calculation, the results in the present thesis are obtained *not* including the semicore states, unless specified otherwise.

3.5 Point defects thermodynamics

3.5.1 Defect formation energies

Defect formation in materials is associated with a change in the Gibbs free energy. The Gibbs free energy of formation is a central property for describing the thermodynamics of a defect in the system and is expressed as

$$\Delta G_f = \Delta E_f + p\Delta V_f - T\Delta S_f. \tag{3.20}$$

The formation free energy is the difference in the free energy of the structure before and after the defect is created. In this process some of the atomic bonds are stretched or broken leading to a change in energy. The formation free energy of a defect is calculated as

$$G^f = G^{\text{defect}} - G^{\text{ideal}} - \sum \Delta n_i \mu_i, \tag{3.21}$$

where G^{defect} is the free energy of the defective system and G^{ideal} is the free energy of the perfect reference cell. The variation of the formation free energy with the chemical environment is given by the last term in Eq. (3.21), which involves the chemical potentials of the constituents. The difference between the number of atoms of type i in the reference cell and the defective cell is denoted by Δn_i , where positive and negative values correspond to the addition and removal of an atom relative to the ideal cell, respectively. Here, we take the chemical potential μ_i of each constituent to be identical to its cohesive energy per atom [60].

For a system in thermal equilibrium, the free energy of the system is minimum, and the dilute limit concentration of the defects is related to the formation free energy via

$$c = c_0 \exp\left(-\frac{\Delta G_f}{k_B T}\right), \tag{3.22}$$

where c is the equilibrium concentration of the defects, c_0 is the concentration of available defect sites, k_B is the Boltzmann's constant, and T is the temperature.

3.5.2 Formation volume tensors

A defect can affect other point as well as line defects (dislocations) either via a direct "chemical" interaction or via long-range elastic interactions. The strain field can modify the saddle points during point defect migration [61]. Similarly, it can affect the barriers for dislocation kink nucleation and growth and thereby affect the plastic behavior [62].

Formation volumes quantify the induced strain in terms of linear elasticity theory and the formation volume tensors provide additional information concerning the orientation and anisotropy of the strain field.

Given the cell metrics of the ideal supercell L_0 and the fully relaxed supercell containing the defect L, the formation volume tensor can be obtained from the relation [63, 64]

$$\begin{aligned} v^f &= \det(L_0) \ln\left(L_0^{-1} L\right) \\ &\simeq \det(L_0)(L - L_0)L_0^{-1}. \end{aligned} \tag{3.23}$$

The formation volume equals one third of the trace of the formation volume tensor. By diagonalizing the formation volume tensor one obtains the orientation and the strength of the strain field. The former is specified by the eigenvectors whereas the latter is related to the magnitude of the eigenvalues. In particular, in Paper I, we considered the anisotropy defined as the ratio of the largest to the smallest eigenvalue.

3.5.3 Defect kinetics

The migration processes of atoms in solids can be described as a sequence of jumps between neighbouring stable sites. In this description the migrating particle spends the majority of the time residing in a potential well, corresponding to a stable position. Collective vibrations of the system can be interpreted as attempts of the particle to break out of the well. If the temperature of the material is sufficiently high, the particle will occasionally succeed crossing a potential barrier and end up in the well corresponding to a neighboring site, see Fig. 3.4.

Fick's first law of diffusion provides a representation of diffusion processes

$$\boldsymbol{J}_i = -D_i \nabla c_i \tag{3.24}$$

in which, $\boldsymbol{J}_i$ is the flux of atoms meaning the number of atoms of kind i passing the unit area perpendicular to the direction of $\mathbf{J}$ per unit time. D is the diffusion coefficient, and ∇c_i is the concentration gradient of atom type i.

Fick's second law of diffusion provides a more complete description of the process by presenting the evolution of concentration with time

$$\frac{\partial c_i}{\partial t} = \nabla(D_i \nabla c_i). \tag{3.25}$$

Here D_i, as the diffusion coefficient of atom type i, can be described by Arrhenius formula

$$D_i = D_{i0} \exp(-E_m/k_B T). \tag{3.26}$$

The pre-exponential factor D_{i0} is related to the lattice geometry and can be obtained by phonon calculations. E_m is the migration energy, which is required for the migrating species to move from the initial potential well to the next one, see Fig. 3.4, [65].

Diffusion can be altered by other processes in the system like interactions between defects and impurities. Such interactions can slow down the mobility of the defect if for instance it becomes trapped by the impurity atom. The binding energy between impurity and point defect is a key factor in understanding defect and solute atom migration.

In the present work, various binding energies are calculated for different types of point defects and impurities. For example the binding energy between impurity and self-interstitial is defined as the difference between the formation energy of mixed-interstitial and the sum of the formation energies of self-interstitial and substitutional defects

$$E_X^b = E^f([X-W])_W - E^f([W-W])_W - E^f(X)_W. \tag{3.27}$$

Note that by this definition, negative (positive) binding energies imply attractive (repulsive) interactions between the defects.

3.5.3.1 Nudged elastic band method

The Nudged elastic band (NEB) is a method to calculate the migration energy. It is an efficient method for finding the minimum energy path (MEP), and the saddle point of the potential energy surface between initial and final configurations of a transition such as chemical reactions and diffusion processes in solids [66].

The method works by minimizing the energy of a number of intermediate images along the MEP. The energy of each image is optimized in a way that all the neighboring images in this string of atoms maintain approximately equal spacing. To achieve this constrained optimization, only the perpendicular component of the true force and the parallel component of spring force are included. The saddle point corresponding to the highest energy along the path represents the activation energy barrier. This barrier enables estimating transition rates within the harmonic transition state theory [67].

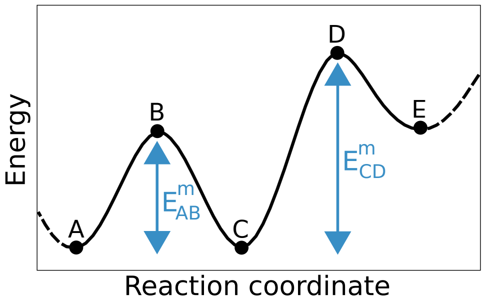

Figure 3.4: Example of potential energy along a migration path. In moving from point A to point E, the particle has to overcome two transition barriers with corresponding barrier heights of E^m_{AB} and E^m_{CD}.

It is important to make sure that the actual saddle point is found, therefore one of the images is made to climb up along the elastic band to converge on the saddle point. This modification is considered in the climbing image NEB (CI-NEB) method [68], which is employed in the calculations of this thesis.

3.6 Atomic scale modeling of alloys

The alloy cluster expansions (CE) approach is a powerful technique for computing thermodynamic properties in multicomponent systems. It is used extensively to determine the energy as a function of different arrangement of atoms over lattice sites. For this purpose a set of configurations is constructed and subsequently used for training the CE. The CE can be subsequently sampled using Monte Carlo (MC) simulations, which enables one to predict, e.g, alloy phase diagrams.

3.6.1 Alloy cluster expansions

An alloy cluster expansion (CE) can be regarded as a generalized Ising model. In atomic scale modeling of alloys, one is usually interested in configurations corresponding to a distribution of M different species over N sites. Each configuration can be described by a vector σ and a property Q of the system can be expressed as [69]

$$Q = \sum_{\alpha} m_\alpha \mathrm{J}_\alpha \left\langle \Gamma_\alpha(\sigma) \right\rangle_\alpha, \tag{3.28}$$

where α and m_α denote a symmetricallu unique cluster and its multiplicity, respectively. The coefficients J_α are referred to as effective cluster interactions (ECIs), and $\Gamma_{\alpha'}$ are cluster functions, which represent the probability of finding cluster α in configuration σ. The last term in the above expression represents the average over all symmetry equivalent cluster functions and the sum runs over all symmetrically distinct clusters (points, pairs, triplets, quadruplets, etc.) [69, 70, 71].

When all clusters α are considered in the sum, Eq. (3.28) is exact [72]. In practice, however, the sum can be truncated due to the fact that interactions decay quickly with distance. ECIs are the unknown quantities of a CE and can be determined by fitting to the energy of a number of configurations obtained through first-principles calculations. The process of CE construction employed in paper V is described in details in the following subsection.

3.6.2 CE construction

In order to determine a certain property of a system, first a suitable set of structures should be selected for training and validation. The most simple way to perform this selection is to randomly choose the structures. This can be done by creating a supercell based on a primitive cell, and decorating it with A and B atoms. The energies of these configurations are then calculated using density functional theory.

However, this is not generally the optimum approach for generating structures, as random structures may fail to sample important parts of configuration space. In particular for larger cells, the probability of e.g., ordered configurations to occur decreases quickly with size.

Instead of randomly selecting the structures, a better approach is to perform a systematic structure enumeration. In this case, one can first start with creating all possible structures that have 2 atoms per unit cell, and then continue with creating all the different structures that contain 3, 4, 5 and more atoms in the unit cell. By increasing the size of the cell the number of structures, which are generated becomes larger. For our calculations, structures up to 12 atoms per unit cell were included, resulting in pools of 10850 structures for BCC and 5777 structures for HCP.

When the structures are selected, the next step is to *train* the CE to match as closely as possible a series of first-principles calculations. In order to perform such training, structures can be selected randomly from the set. An alternative, more refined approach compared to the random approach is to calculate all the cluster vectors for all the structures in the selection database and then pick them such that these cluster vectors are as orthogonal to each other as possible. One way of achieving that is to choose the cluster vectors to all lie on a hypersphere [73]. For the calculations in the present thesis a random selection has been performed.

In order to train a CE, a linear algebra problem of the following form should be solved

$$\bar{\mathbf{\Pi}}\,\mathbf{J} = \boldsymbol{Q}, \tag{3.29}$$

where $\bar{\mathbf{\Pi}}$ is called the sampling matrix, which is obtained by stacking the vectors that represent the clusters present in each structure of the training set, i.e. $\langle \Gamma_\alpha(\sigma) \rangle_\alpha$ in Eq. (3.28), $\mathbf{J}$ represents ECIs, and $\boldsymbol{Q}$ is the vector of target properties of interest, such as energy.

If the CEs are constructed conventionally, the number of elements in $\boldsymbol{Q}$ is much larger than the number of ECIs. The set of equations is thus overdetermined. The optimal set of ECIs for fixed training set and cluster function basis is then obtained by minimizing the l_2-norm of $\bar{\mathbf{\Pi}}\,\mathbf{J} - \boldsymbol{Q}$

$$\mathbf{J}_{\text{opt}} = \arg\min_{\mathbf{J}} \left\{ ||\, \bar{\mathbf{\Pi}}\,\mathbf{J} - \boldsymbol{Q}\, ||_2 \right\}. \tag{3.30}$$

A series of CEs corresponding to different basis set choices are then generated using common algorithms [69]. By comparing the performance of each CE by means of its Cross Validation Score (CVS) the best performing CE is selected.

An alternative approach is to solve an underdetermined problem, where the number of structures available for fitting in $\boldsymbol{Q}$ is much smaller than the number of ECIs, and the solution obtained is consequently not unique. This alternative approach, which offers considerable advantages with regard to accuracy, transferability as well as efficiency, is based on the compressive sensing (CS) technique [74]. There are different algorithms to solve compressing sensing problems like LASSO (least absolute shrinkage and selection operator) and split-Bregman. The latter is the algorithm used in our calculations to find the ECIs.

When a fit has been performed it should be validated so that the ECIs are actually useful. To evaluate a CE a Cross Validation Score (CVS) can be used. The simplest form is the Leave-One-Out (LOO) CVS. Another way of evaluation the parameters used for the fitting algorithm is called sampling. By sampling, one samples many different choices on the training and validation set, and then takes an average over the root mean square errors of the validation sets.

After training and validation are done, it is time for the *analysis of the results*. For our calculations we analyzed average and standard deviation of the mixing energy vs concentration over the set of CEs that was obtained.

To obtain the final CE, the ECIs were averaged, after which clusters were removed for which the average ECI was smaller than half the standard deviation. In this fashion, statistically insignificant CEs were removed, leading to a smaller CE.

3.6.3 Monte-Carlo simulations

Once the CE is found to be satisfactory, the configuration space can be sampled using Monte Carlo (MC) simulations. In order to determine thermodynamic properties of alloys, a convenient way is to sample the semigrand canonical ensemble when performing a MC simulation. The semigrand canonical ensemble is defined as an intermediate between the canonical and grand canonical ensembles, in which the total number of particles and the difference in chemical potential of the species are fixed, i.e. N_{tot}, $\Delta\mu$, V, and T are constant. It is straightforward to calculate the free energy from $\Delta\mu$ and c in this ensemble, however it has a major disadvantage when it comes to alloys with constituents that do not mix in all concentrations (immiscible systems). Since sampling of the free energy landscape inside the miscibility gap is not possible. For analyzing the W-Ti phase diagram in Paper V, we, however, require the free energy landscape for BCC and HCP phases as a *continuous* function of composition. This prevents us from using the semi-grand canonical (SGC) ensemble since it does not allow sampling multiphase regions, which are present for both BCC and HCP lattices.

To overcome this limitation the variance-constrained semigrand canonical (VCSGC) ensemble, has been proposed. This approach includes an additional term in the partition function that effectively imposes a constraint on the fluctuations of the concentration, which diverge in multi-phase regions. The VCSGC ensemble is sampled by randomly selecting a site in the system, swapping its chemical identity, and accepting this trial move with probability [75]

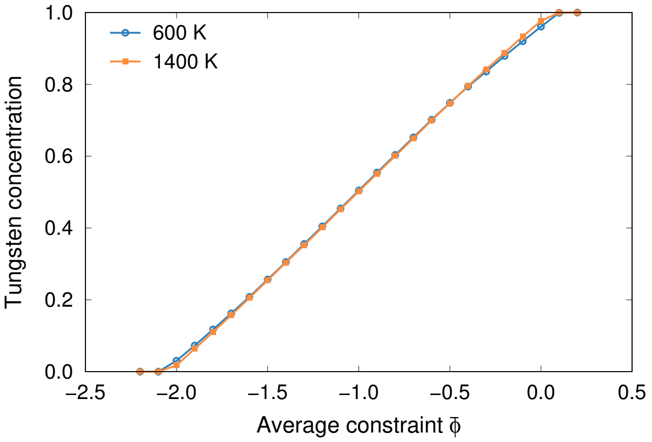

Figure 3.5: Tungsten concentration vs. ϕ parameter for BCC phase at temperatures 600 K and 800 K. Figure is generated from the calculations of the present work.

$$\mathscr{P} = \min[\exp[-\beta\Delta E - \kappa\Delta N_B\left(\phi + \Delta N_B/N + 2N_B/N\right)]].$$

Here, ΔE is the energy change associated with the move, ΔN_B is the change in the number of particles of type B, N is the total number of sites (atoms) in the simulation cell, and ϕ and κ are the average and variance constraint parameters.

In several previous works, it has been shown that the variance constraint parameter κ can be chosen from a rather wide range, typically $100 \lesssim \kappa \lesssim 1000$. It must be chosen large enough to stabilize the system inside the miscibility gap and small enough not to affect the acceptance rate too negatively. The precise value for κ is, however, not very critical and values between 100 and $\lesssim 500$ have been found to work regardless of the system. The average constraint parameter ϕ can then be varied in steps of 0.02 from -2.2 to 0.2 to sample the entire concentration range. Figure 3.5 shows tungsten concentration vs. ϕ parameter for BCC phase at temperatures 600 K and 1400 K.

In the VCSGC ensemble the first derivative of the free energy is related to the (ensemble) average of the concentration $\left\langle c_B \right\rangle = \left\langle N_B \right\rangle / N$,

$$\beta\partial\Delta F/\partial c = \kappa\left(\phi + 2\left\langle c_B \right\rangle\right), \tag{3.31}$$

which allows one to obtain the free energy of mixing.

From Eq. (3.31) one can obtain the first derivative of the mixing free energy with respect to concentration. Here, $\partial\Delta F/\partial c \simeq \partial\Delta G/\partial c$, since the volume-pressure term is small (In our calculations, ionic and cell relaxations are implicitly included in the ECIs.). For a binary alloy, $\partial\Delta G/\partial c$ corresponds to the chemical potential difference between the two species, see Fig. 3.6 (a). Chemical potential difference can be further integrated using for example the trapezoidal rule, to yield the mixing free energy. In order to construct the free energy landscape, all different phases of the system (stable and metastable) should be considered.

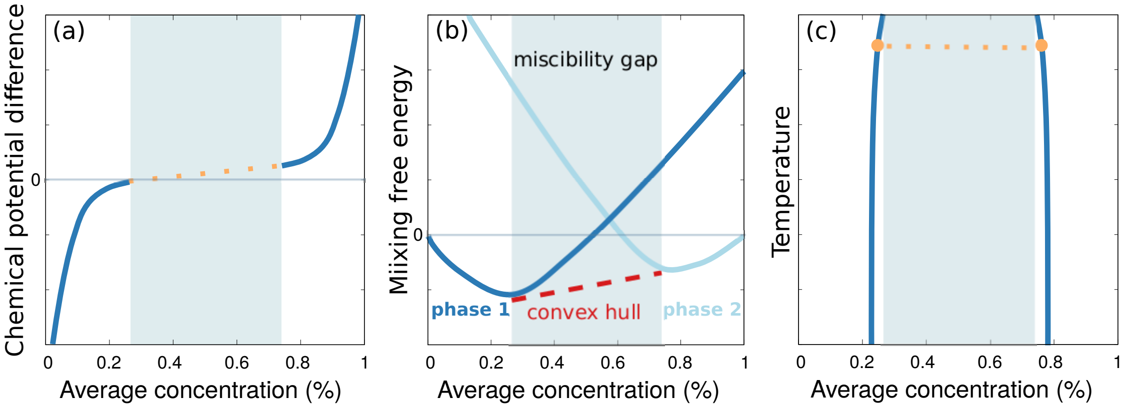

Figure 3.6: Schematic illustration of the steps for a phase diagram construction, for a binary system with a miscibility gap. General steps include (a) extracting the chemical potential difference vs. concentration, (b) constructing the convex hull of the mixing free energies, and (c) constructing the temperature-concentration phase diagram. A certain temperature corresponding to the convex hull shown in (b) is marked using orange dots in the phase diagram in (c).

After having determined the free energies of all phases (like BCC and HCP phases for the W-Ti system), one can construct the full temperature, composition, and structure dependent free energy landscape, from which the phase diagram can be extracted. To this end, the free energies for the different phases should be combined to construct a convex hull. Fig 3.6 (b) shows the mixing energy of two phases of a system at a certain temperature, for which the convex hull is constructed and shown with a dashed red line. The convex hull is then obtained for a temperature range and will be used to construct a temperature vs. concentration phase diagram, see Fig 3.6 (c). A certain temperature corresponding to the convex hull shown in Fig. 3.6 (b) is marked using orange dots in the phase diagram in Fig. 3.6 (c).

4

Results and conclusion

4.1 Point defects and radiation-induced precipitation

Tungsten is a prime candidate for applications in fusion reactors as a first wall material, thus understanding its behavior under irradiation is crucial. It has been observed that needle-shaped Re-precipitates are formed in W and W–Re alloys under irradiation, at Re concentrations well below the solubility limit [76]. Formation of such precipitates can alter the mechanical properties of tungsten and can lead to alloy hardening and thermal conductivity losses [76, 77].

In papers I-III, we conducted a study in order to understand the mechanisms by which, nonequilibrium clusters of solute atoms are formed under irradiation. I started this study by calculating the basic properties of individual mixed-interstitials and further extended the study to di-interstitials and their interactions. For higher concentrations, defects mixing energies in tungsten were studied as well. We also determined the energy landscape for interstitial and vacancy diffusion. Using all these information, our collaborators constructed a kinetic Monte Carlo (kMC) model. This model provides a quantitative description of processes that are important for the actual irradiation process in terms of the formation of Re precipitates. Results from these three papers show that there are different regimes during formation and evaluation of these precipitates. Besides the vacancy drag mechanism, interstitials also contribute to cluster formation while the mutual coupling of these fluxes is responsible for the initial defect accumulation.

4.1.1 Paper I

In paper I, by means of first-principles atomistic methods based on density functional theory (DFT), an extensive convergence study was performed first, to understand the effect of Brillouin zone sampling, size dependence, and semicore states on defect energetics. The results were

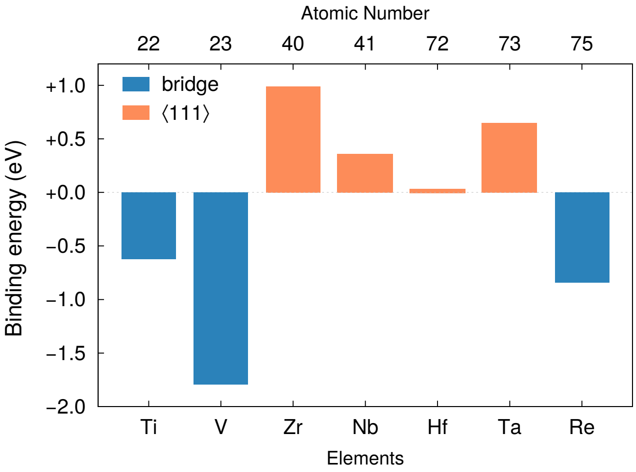

Figure 4.1: Binding energies between self-interstitial atoms and substitutional solute atoms relative to the respective most stable mixed-interstitial configuration. The figure is from paper I of the present thesis [78].

further used to calculate the properties of a number of solute atoms in tungsten in the dilute limit.

Interstitial defects possess positive large formation energies and are practically absent in equilibrium. They are, however, important under reactor relevant conditions. Mixed-interstitials are formed under irradiation after self-interstitial atoms (SIAs) diffuse through the lattice and become trapped by solute atoms. The binding energy was found to be very strong (~-0.6 to -1.8 eV) for Re, Ti, and V, indicating that thermal de-trapping was unlikely, see Fig. 4.1. Such interactions are important for materials under irradiation as they cause a reduction in interstitials mobility, which can accelerate damage build-up. Trapping is a precursor to segregation and may eventually lead to solute precipitation.

In addition to trapping, Re, Ti, and V mixed-interstitials were found to exhibit a pronounced anisotropy[1] in the defect formation volume tensor and possess not only strong but very anisotropic strain fields. The highly anisotropic nature of these interstitials further raise the question of possible defect-defect interactions especially at high concentrations. Such interactions may lead to the creation of separated phases in the material, which will eventually influence, for example the mechanical properties. In the next step, I therefore focused on understanding defect-defect interactions.

---

[1] Anisotropy is quantified by the ratio between the largest and smallest eigenvalues of the formation volume tensor.

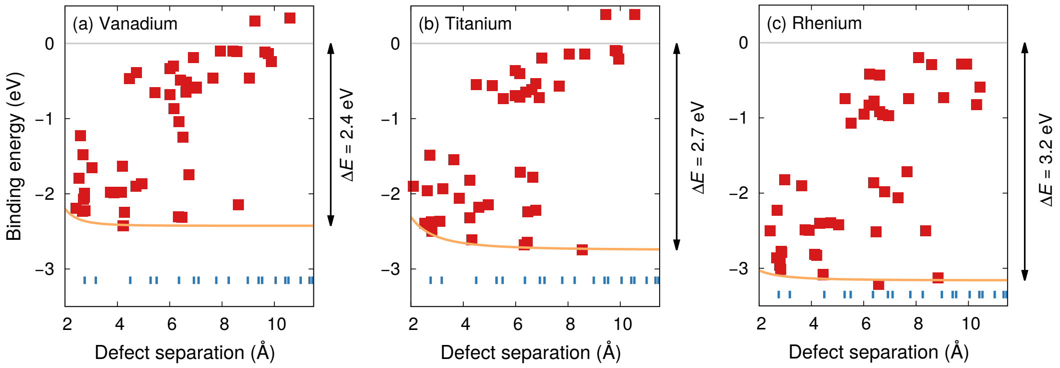

Figure 4.2: Binding energy between two (a) V–W, (b) Ti–W, and (c) Re–W mixed interstitials as a function of pair separation. The blue tics indicate the positions of the neighbors shells in the perfect structure. The solid orange lines represent the repulsive interaction between two substitutional extrinsic atoms referred to the most strongly bound configuration. The figure is from paper II of the present thesis [79].

4.1.2 Paper II

In paper II, the behavior of di-interstitial was investigated considering Re, Ti, and V mixed-interstitials. We demonstrated that these mixed-interstitials are strongly attracted to each other with binding energies of several eV, see Fig 4.2.

We found that after mixed-interstitials were formed due to trapping, they were able to diffuse further via low-energy rotations and translations while dragging the solute atom along. Our results showed that a mobile mixed-interstitial atom could further meet another mixed-interstitial, bind strongly and become aligned. Throughout such a process, mixed-interstitials, via a 3D diffusion mechanism, can effectively transport solutes over long distances and, considering the large binding energy between di-interstitials, this could eventually result in clustering. These mixed di-interstitials are kinetically very stable due to their strong binding energies, which makes them preferential sites for more defect absorption. While additional interstitials approaching these small clusters may not be initially aligned, they are energetically favored to again rotate into alignment, increasing cluster size and forming a precipitate nucleus via interstitial accumulation.

To provide more evidence for the tendency of the system for interstitial agglomeration, I calculated the mixing energy of the defects. The mixing energy for interstitials is found to be positive and concentration dependent. It was shown to feature a maximum at about 15% and approach zero at approximately 30%. This suggests that if the concentration of mixed-interstitials reaches a concentration of $\gtrsim 30\%$, the structure becomes (locally) unstable and can transit into substitutional configurations.

The mechanism described above cannot on its own account for the radiation-induced precipitation observed in W–Re alloys since, e.g. in the real system vacancy migration will play a role. In paper III we extended our study by implementing the energetics and mechanisms presented

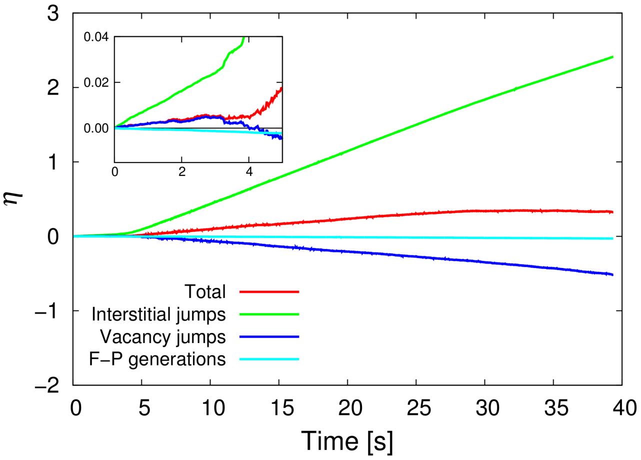

Figure 4.3: Evolution of the differential SRO during the nucleation and growth in the kMC simulations. The figure is from paper III of the present thesis [80].

here into a kMC model enabling us to suggest a more comprehensive mechanism for formation of Re precipitates in tungsten.

4.1.3 Paper III

In paper III, we investigated the mechanism that governs the formation of Re-rich clusters in tungsten. Such clusters are formed under high-temperature, high-dose neutron irradiation, at concentrations well below the solubility limit. They may eventually transform into brittle W–Re intermetallic phases, which can lead to high levels of hardening and thermal conductivity losses. Understanding the mechanism by which nonequilibrium clusters are formed under irradiation is crucial for predicting materials degradation and devise mitigation strategies. To this end, I carried out DFT calculations for the W–Re system and characterized the landscape for diffusion. My results were subsequently used by collaborators to parametrize a kMC model.

On the basis of our results, the sequence of events that leads to the formation of Re-rich precipitates in irradiated W–2Re (at%) alloys was found to be as follows. The process starts with inserting a Frenkel pair in the system, and after which interstitial and vacancy diffuse around. Interstitials perform a one dimensional (1D) diffusion in the system until they encounter an impurity atom, bind and form a mixed-interstitial. At this point interstitials are capable of transporting solute atoms in three dimensions (3D). Mixed-interstitial migration continues until mixed-interstitials encounter more impurities and become trapped. These solute–mixed-interstitials are now firmly bound and effectively immobile.

Vacancies also diffuse, eventually become trapped, and form small Re-vacancy complexes. These Re-vacancy complexes continue to grow. At high temperatures, however, vacancies can de-trap and continue migrating until they find immobilized interstitials and become trapped forming another small V-Re cluster. Throughout this process, both mixed-interstitial and vacancy hops contribute to an increasing SRO parameter, see Fig. 4.3.

Eventually one Re cluster grows larger than the rest, due to natural fluctuations. At this point the probability of vacancy–mixed-interstitial annihilation increases and the cluster growth continues by attraction of mixed-dumbbells. At this stage, vacancies reverse their role as solute-atom 'hinges' and begin to contribute to cluster dissolution. The differential SRO parameter decreases and becomes negative at this point, see Fig. 4.3.

While the precipitate continues to be the main pole of attraction for vacancy-interstitial recombinations, the system reaches a saturation point where most of the solute is consumed and the cluster stops further growth. In the absence of sinks or other precipitates, the existing cluster is the only focus of solute agglomeration, which allows it grow to its maximum possible size considering the Re content. During this saturation step the total differential SRO parameter flattens out, see Fig. 4.3. If there are competing solute sinks in the system, it is expected that the size of the precipitate would be comparably smaller or it is less solute-dense internally.

4.2 Description of thermophysical properties in density functional theory

4.2.1 Paper IV

I conducted my earlier calculations (Papers I-III) using the GGA functional PBE [48]. PBE is one of the most successful general-purpose functionals for systems with dense electron distributions like hard materials and metals. The accuracy of PBE, however, is limited as it, e.g., systematically overestimates lattice constants and usually underestimates the mechanical stiffness (elastic constants).

In paper IV, I therefore compared the performance of a number of commonly used constraint-based exchange-correlation functionals and studied structural and thermophysical properties of non-magnetic transition metal elements. Compared to other assessments, I specifically included vibrational effects, which are much expensive to evaluate but provide a more rigorous benchmark than energies alone.

Specifically I focused on constraint-based functionals and considered the new consistent-exchange van der Waals density functional version vdW-DF-cx, the semi-local PBE and PBEsol functionals as well as the AM05 meta-functional. Using the quasi-harmonic approximation, structural parameters, elastic response, and thermal expansion at finite temperatures were computed and compared to experimental data. I also computed cohesive energies explicitly including zero-point vibrations.

It was shown that overall vdW-DF-cx provides an accurate description of thermophysical properties and retains a level of transferability and accuracy that is at least comparable and usually better than the other functionals considered in this study. This demonstrates that vdW-DF-cx has general-purpose character and can be used to study systems that have both sparse and dense electron distributions.

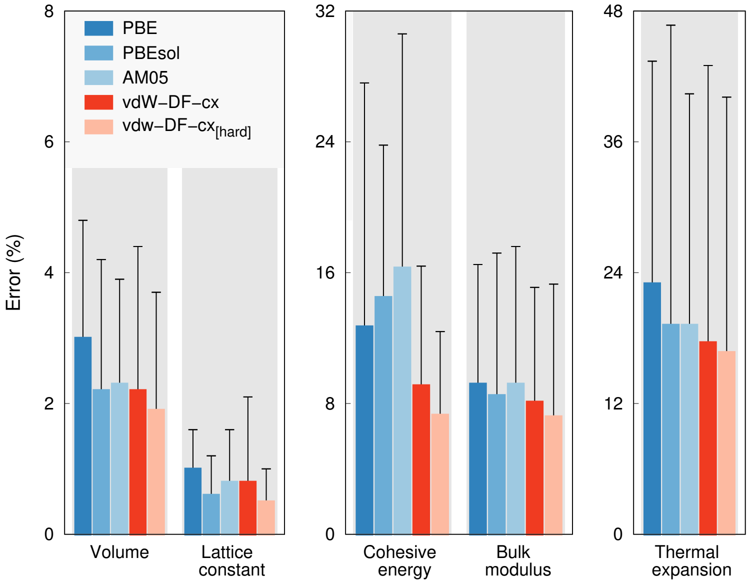

Figure 4.4: Performance of different constraint-based exchange-correlation functionals. Errors on the y-axis represent the mean average percentage errors (MAPEs), which were computed with regard to thermophysical properties measured at 300 K, with the exception of the cohesive energy, for which zero K values are compared. Standard deviations of the distribution of errors for each property and functionals are shown as black error bars. The figure is from paper IV of the present thesis [81].

4.3 W–Ti phase diagram

My prior calculations on different alloys suggested to take a closer look at W–Ti system. In paper I, the Ti substitutional formation energy was found to be negative indicating a tendency to form a solid solution with tungsten. In paper II, I showed furthermore that the mixing energy for the BCC solution is negative, which could result in an extended miscibility range. It was furthermore demonstrated that the W–Ti system exhibits a balance between HCP and BCC in terms of elemental reference structures and their energetics compared to W–V and W–Re systems. In addition, due to experimental difficulties, the existing low temperature phase diagrams of W–Ti system are based on a sparse set of data, which motivated a further investigation of this system.

In paper V, we established the low-temperature behavior of the W–Ti system especially on the W-rich side and showed that the asymmetric solubility results from the balance of stable and metastable lattice structures.

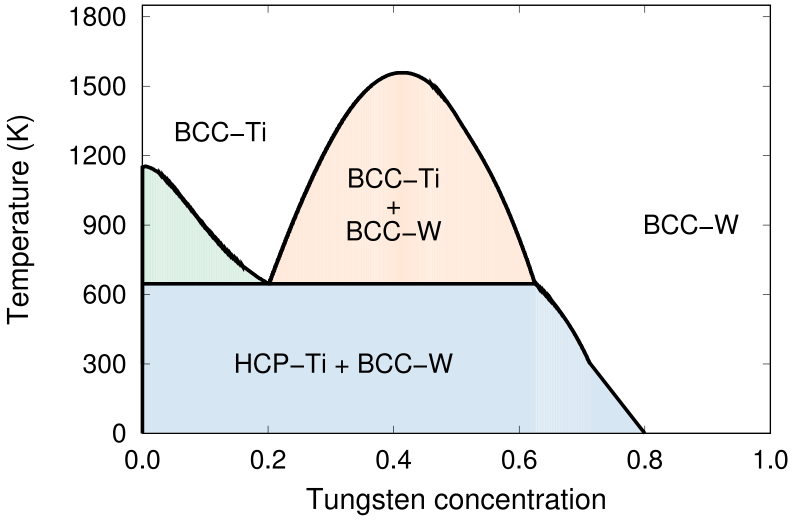

Figure 4.5: Phase diagram predicted based on the simulations in the present work in comparison with experimental data points and previous thermodynamic assessments. The figure is from paper V of the present thesis [82].

4.3.1 Paper V

Phase diagrams for the multi-component systems are very important since they represent crucial information for understanding and designing materials. They are, however, very time consuming to assess experimentally. In this work, we focused on the W–Ti binary alloys. For the W–Ti system, because of the high melting point of tungsten and the accompanying slow kinetics, the systematic exploration of the phase diagram, in particular on the W-rich side, has been very cumbersome. Since experimental data points for tungsten concentrations $\gtrsim$ 30% are only available down to 1473 K, the W–Ti system had been assessed using rather severe assumptions and need to be readdressed [83, 84, 85, 86, 87].

Using computational methods, the phase diagram of a binary alloy can be derived theoretically. In this regard, the type of interactions between the species in the system should be considered. If the interaction between the two constituents is repulsive (attractive) the system shows positive (negative) mixing energy. This interaction between the constituents is usually symmetric, in the sense that if A dissolves in B, so does B in A. One exception from this behavior is the Fe-Cr system, which has probably been studied the most extensively due to its technological importance. In the Fe–Cr system, Cr has been shown to be more soluble in Fe-rich side. The mixing energy goes through a sign inversion and the system features a broad miscibility gap. As a result of sign inversion in the mixing energy, the phase diagram is very asymmetric with a large solubility on the Fe-rich and a very small solubility on the Cr-rich side. This behavior, which at first sight might be unexpected given a very small size mismatch and identical lattice structures, can be rationalized in terms of the magnetic structure with Fe and Cr preferring ferro and antiferromagnetic ordering, respectively [88, 89, 90].

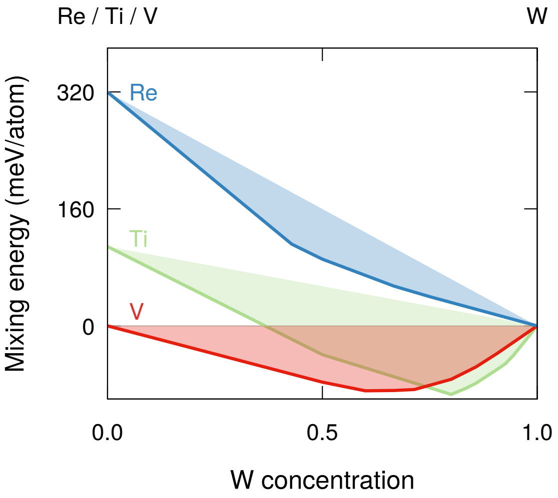

Figure 4.6: Schematic illustration of mixing energies for BCC structures of W–V, W–Ti, and W–Re based on data from paper II [79]. In the case of the latter two alloys, the energy offset in the Ti/Re-rich limit represents the HCP-BCC energy difference. The figure illustrate that the occurrence of a finite solubility at zero temperature in the case of W–Ti is the result of a combination of a negative mixing energy on the BCC lattice and not-too-large HCP-BCC energy difference.

In paper V, we showed that the phase diagram of W–Ti system was also strongly asymmetric for a different reason. In the non-magnetic W–Ti alloy, asymmetric phase diagram was found to emerge as a result of an asymmetry in lattice structures and their energetics.

The W–Ti binary alloy, at ambient conditions, comprises two different crystallographic phases, a BCC phase and a HCP one. The BCC phase is the most stable phase in the W-rich limit for low temperatures up to the melting point. The HCP phase prevails in the Ti-rich limit up to moderately high temperatures. In paper V, the mixing energies on both the BCC and HCP lattices were described using lattice models, specifically alloy cluster expansions (CEs). The CEs were sampled using Monte Carlo (MC) simulations in the variance constrained semi-grand canonical (VCSGC) ensemble, and thermodynamic data for the pure elements were taken from Ref. [91].

We demonstrated that the mixing energy on the BCC lattice is actually negative. This is in contrast to previous thermodynamic assessments based on experimental data, which have assumed a positive mixing energy over the entire composition range. This positive mixing energy was then found to be important for describing the low temperature solubility limit especially on the W-rich side. We showed that the solubility of Ti in W exceeds 20% down to zero temperature in stark contrast to previous thermodynamic assessments, while the inverse solubility is practically zero up to the HCP-BCC transition, see Fig. 4.5.

We concluded that such asymmetry in the phase diagram of the W–Ti system can be traced to the energy balance between BCC and HCP structures, which are stable and metastable, respectively, on opposite ends of the phase diagram. It is important to note that while the low temperature regions of the phase diagrams of refractory metals are exceedingly difficult to sample in equilibrium, they are nonetheless relevant as they determine the driving forces under extreme non-equilibrium situations such as encountered during ion irradiation.

While our findings in the present paper pertain to our understanding of the W–Ti phase diagram, it has shown to have more general implications for alloy thermodynamics. Binary phase diagrams of metals that exhibit strongly asymmetric solubility limits are relatively rare. While as mentioned above in the case of the Fe–Cr system, they can arise from competing forms of magnetic order, we showed that this effect can also be observed in non-magnetic systems as a result of different lattice structures.

To illustrate this effect further, we considered two systems including W–V (BCC) and W–Re (BCC and HCP) in comparison with W–Ti (Fig. 4.6; data from paper II [79]). We showed that the W–Ti system emerges as an intermediate case compared to W–V and W–Re in terms of elemental reference structures and their energetics. V adopts a ground state BCC lattice and due to the difference in lattice constant at ambient conditions between W and V, the mixing energy was shown to be slightly asymmetric yet negative throughout the entire composition range.

As for Ti, the mixing energy of W–Re on the BCC lattice was shown to be negative but slightly positive for HCP (Fig. 5(c) from paper II). The HCP-BCC (free) energy difference for Re is, however, even larger than for Ti. As a result, the negative mixing energy of the BCC lattice is shifted upward such that the solubility of Re in BCC-W is very small and approaches zero with vanishing temperature.

The comparison with W–V and W–Re demonstrated that the occurrence of an asymmetric phase diagram in W–Ti is the result of a structural asymmetry on one hand and the rather small energy difference between BCC-Ti and HCP-Ti on the other hand. In turn, this implies that similar behavior can be expected in systems that combine different lattice structures, in particular if they are metastable.

4.4 Conclusion and outlook

In papers I-III, I performed extensive DFT calculations, which ultimately led to the parametrization of a new model for explaining the formation of W–Re precipitates (paper III). This model provides an improved understanding of the processes that are important for the actual irradiation process in terms of the formation of Re precipitates. Our results show that there are different regimes during formation and evaluation of W–Re precipitates. Besides the vacancy drag mechanism, interstitials also contribute to cluster formation while the mutual coupling of these fluxes is responsible for the initial defect accumulation. Understanding the mechanisms by which such nonequilibrium clusters form under irradiation is crucial to predict materials degradation and devise mitigation strategies.

In paper IV, I studied structural and thermophysical properties of non-magnetic transition metal elements employing a number of commonly used constraint-based exchange-correlation functionals as well as the vdW-DF-cx functional. I demonstrated that the vdW-DF-cx functional provides an accurate description of the mentioned properties and its performance is at least comparable and usually better than that of the commonly used exchange-correlation functionals in the literature.

In paper V, I obtained the phase diagram of the W–Ti system and proposed a revision of the W-rich end of the phase diagram. Specifically it was shown that the solubility of Ti in BCC-W is much larger than predicted previously. Finally, by comparison with the W–V and W–Re systems, I demonstrated that structural asymmetry and energy balance of stable and metastable lattice structures are two important factors that can give rise to strongly asymmetric phase diagrams.

First and foremost, the results presented in this thesis provide an improved understanding of the W alloys. There are, however, still a number of areas that need to be addressed in the future. One interesting direction is a further investigation of the plastic deformation mechanisms in tungsten alloys. One of the concerns regarding the performance of tungsten as a structural material in fusion reactors, is the high brittle to ductile transition temperature of tungsten. The ductility of tungsten has been shown to be controlled by the mobility of screw dislocations and alloying of tungsten either intentionally or via transmutation alters this behavior [15, 30]. This area deserves to be investigated further.

Tungsten oxides are also relevant for understanding the performance tungsten in fusion reactors, as they are formed in the case of a breach of the reactor shell or reactor melt down. In such situations, tungsten readily forms oxides during air ingress into the vacuum vessel [92]. Among the tungsten oxides, tungsten trioxide is known to form a porous surface layer that cannot prevent continuous oxidation of the underlying metal. Understanding the mechanism of oxidation and which oxides of tungsten are formed should therefore be considered in the future work.

Acknowledgments

I would first of all like to express my sincere gratitude to my supervisor, Paul Erhart. Thank you for giving me the opportunity to pursue this work and follow my dream of being a researcher. Your enthusiasm, immense knowledge, patience and continues support have always been a great help during my PhD studies. Thank you also for the instructive and fun experience of being your teaching assistant, I enjoyed it and learned a lot during that time. It was such a joy to start as the first PhD student in the group and see how the group grew and got stronger over the past five years. I also appreciate a lot the opportunity of having frequent meetings that did not change as the group grew, it was a great relief that I could always count on. I don't have more words to express my appreciation but to say *Ich danke dir sehr PAUL!*

I also would like to thank my examiner Göran Wahnström for discussions, professional advise and constructive comments. I learned a lot during the group meetings you arranged every week, and it was also so much fun joining our group activities. I will miss those a lot.

I acknowledge support from the Swedish Research Council and the European Research Council as well as computer time allocations by the Swedish National Infrastructure for Computing at NSC (Linköping), C3SE (Gothenburg), and PDC (Stockholm).

All my past and present colleagues should be thanked for making Origo Plan 7 a creative and positive environment. My special thanks goes to the ones at *joyful* Tuesday Fikas and Wednesday *Foxes* time! Thank you Mattias, Erik F, Magnus, Christopher, Anders, Erik J, Narjes, Joakim and Fredrik for all the fun talks sometime leading to challenging bets!, cheese and pepperoni half-pizzas, and suggestions on TV series. Well I might watch Game of Thrones one day! Still can't promise! I also would like to thank Daniel for the time we shared office, for long interesting discussions, dividing students assignments and hope they wouldn't pick the last one!

This is a great opportunity to acknowledge all the significant individuals without whom and their support and inspiration it was impossible for me to be here at this very moment. My friends here in Sweden and back in Iran. Azadeh, Samira, Siavash, Alireza, Jeroen and all my friends. You all mean a lot to me, and every one of you brought your own light and color into my life and shaped priceless memories for me.

This thesis is dedicated to my family. My deepest appreciation goes to my mom Farzaneh and my dad Mohammad, for truly unconditional love and support, for being my first teachers and leading me to the world of science and literature, and to my sister, my the other half, Shaili, for all the joys and happy moments we share. And finally David, thank you for your patience, love and support especially in the past few months and for sharing your fun and exciting world with me.

Bibliography

[1] A. Stukowski, *Visualization and analysis of atomistic simulation data with OVITO–the Open Visualization Tool*, Modelling and Simulation in Materials Science and Engineering **18**, 015012 (2010).

[2] F. Sartori, G. De Tommasi, and F. Piccolo, *The joint European torus*, Control Systems, IEEE **26**, 64 (2006).

[3] R. Aymar, P. Barabaschi, and Y. Shimomura, *The ITER design*, Plasma Physics and Controlled Fusion **44**, 519 (2002).

[4] *ITER*, `https://www.iter.org`.

[5] D. Maisonnier, I. Cook, S. Pierre, B. Lorenzo, D. P. Luigi, G. Luciano, N. Prachai, and P. Aldo, *DEMO and fusion power plant conceptual studies in Europe*, Fusion Engineering and Design **81**, 1123 (2006), proceedings of the Seventh International Symposium on Fusion Nuclear Technology ISFNT-7 Part B Proceedins of the Seventh International Symposium on Fusion Nuclear Technology.

[6] M. Gilbert, S. Dudarev, S. Zheng, L. Packer, and J.-C. Sublet, *An integrated model for materials in a fusion power plant: transmutation, gas production, and helium embrittlement under neutron irradiation*, Nuclear Fusion **52**, 083019 (2012).

[7] H. Bolt, V. Barabash, G. Federici, J. Linke, A. Loarte, J. Roth, and K. Sato, *Plasma facing and high heat flux materials–needs for ITER and beyond*, Journal of Nuclear Materials **307**, 43 (2002).

[8] W. Wampler and R. Doerner, *The influence of displacement damage on deuterium retention in tungsten exposed to plasma*, Nuclear Fusion **49**, 115023 (2009).

[9] V. Philipps, *Tungsten as material for plasma-facing components in fusion devices*, Journal of Nuclear Materials **415**, S2 (2011).

[10] K. Tobita, S. Nishio, M. Enoeda, M. Sato, T. Isono, S. Sakurai, H. Nakamura, S. Sato, S. Suzuki, M. Ando, K. Ezato, T. Hayashi, T. Hayashi, T. Hirose, T. Inoue, Y. Kawamura, N. Koizumi, Y. Kudo, R. Kurihara, T. Kuroda, M. Matsukawa, K. Mouri, Y. Nakamura, M. Nishi, Y. Nomoto, J. Ohmori, N. Oyama, K. Sakamoto, T. Suzuki, M. Takechi, H. Tanigawa,

K. Tsuchiya, and D. Tsuru, *Design study of fusion DEMO plant at JAERI*, Fusion Engineering and Design **81**, 1151 (2006), proceedings of the Seventh International Symposium on Fusion Nuclear Technology ISFNT-7 Part B, Proceedings of the Seventh International Symposium on Fusion Nuclear Technology.

[11] M. Rieth, S. Dudarev, S. Gonzalez de Vicente, J. Aktaa, T. Ahlgren, S. Antusch, D. Armstrong, M. Balden, N. Baluc, M.-F. Barthe, *et al.*, *Recent progress in research on tungsten materials for nuclear fusion applications in Europe*, Journal of Nuclear Materials **432**, 482 (2013).

[12] *Yielding and fracture in tungsten and tungsten-rhenium alloys*, Journal of the Less Common Metals **17**, 133 (1969).

[13] M. Kaufmann and R. Neu, *Tungsten as first wall material in fusion devices*, Fusion Engineering and Design **82**, 521 (2007), proceedings of the 24th Symposium on Fusion Technology SOFT-24.

[14] T. Tietz and J. Wilson, *Behavior and Properties of Refractory Metals* (Stanford University Press, USA, 1965).

[15] P. Gumbsch, J. Riedle, A. Hartmaier, and H. F. Fischmeister, *Controlling Factors for the Brittle-to-Ductile Transition in Tungsten Single Crystals*, Science **282**, 1293 (1998), Article-Type: research-article / Full publication date: Nov. 13, 1998 / Copyright (C) 1998 American Association for the Advancement of Science.

[16] G. Cottrell, R. Pampin, and N. Taylor, *Transmutation and phase stability of tungsten armor in fusion power plants*, Fusion Science and Technology **50**, (2006).

[17] T. Tanno, A. Hasegawa, M. Fujiwara, J.-C. He, S. Nogami, M. Satou, T. Shishido, and K. Abe, *Precipitation of Solid Transmutation Elements in Irradiated Tungsten Alloys*, Materials Transactions **49**, 2259 (2008).

[18] A. Hasegawa, M. Fukuda, T. Tanno, and S. Nogami, *Neutron Irradiation Behavior of Tungsten*, MATERIALS TRANSACTIONS **54**, 466 (2013).

[19] G. S. Was, *Fundamentals of radiation materials science* (Springer, USA, 2007).

[20] *Radiation damage in materials*, `http://www.acclab.helsinki.fi/~knordlun/rad_dam_course`.

[21] N. Matsufuji, A. Fukumura, M. Komori, T. Kanai, and T. Kohno, *Influence of fragment reaction of relativistic heavy charged particles on heavy-ion radiotherapy*, Physics in Medicine and Biology **48**, 1605 (2003).

[22] S. C. White and M. J. Pharoah, *Oral radiology: principles and interpretation* (Elsevier Health Sciences, USA, 2014).

[23] M. I. Hoffert, K. Caldeira, G. Benford, D. R. Criswell, C. Green, H. Herzog, A. K. Jain, H. S. Kheshgi, K. S. Lackner, J. S. Lewis, *et al.*, *Advanced technology paths to global climate stability: energy for a greenhouse planet*, Science **298**, 981 (2002).

[24] H. G. Graetzer, *Discovery of nuclear fission*, American Journal of Physics **32**, 9 (1964).

[25] M. STEINBRüCK, A. Meier, E. Nold, and U. Stegmaier, *Degradation and oxidation of B4C control rod segments at high temperatures*, Wissenschaftliche Berichte FZKA **6980**, (2004).

[26] D. A. Petti, Z. Martinson, R. Hobbins, C. Allison, E. Carlson, D. Hagrman, T. Cheng, J. Hartwell, K. Vinjamuri, and L. Seifken, Technical report, Nuclear Regulatory Commission, Washington, DC (USA). Div. of Systems Research; EG and G Idaho, Inc., Idaho Falls, ID (USA) (unpublished).

[27] K. Miyamoto, Technical report, National Inst. for Fusion Science, Toki, Gifu (Japan), Japan (unpublished).

[28] J. A. Bittencourt, *Fundamentals of plasma physics* (Elsevier, USA, 2013).

[29] Y. Wu, *Design analysis of the China dual-functional lithium lead (DFLL) test blanket module in ITER*, Fusion Engineering and Design **82**, 1893 (2007), proceedings of the 24th Symposium on Fusion Technology SOFT-24.

[30] D. Hull and D. J. Bacon, *Introduction to Dislocations*, 4th ed. (Butterworth-Heinemann, UK, 2001).

[31] S. J. Zinkle and N. M. Ghoniem, *Operating temperature windows for fusion reactor structural materials*, Fusion Engineering and Design **51**, 55 (2000).

[32] S. P. Fitzgerald and D. Nguyen-Manh, *Peierls Potential for Crowdions in the bcc Transition Metals*, Physical Review Letters **101**, 115504 (2008).

[33] C. Becquart and C. Domain, *An object Kinetic Monte Carlo Simulation of the dynamics of helium and point defects in tungsten*, Journal of Nuclear Materials **385**, 223 (2009).

[34] R. S. Averback and T. Diaz de la Rubia, *Displacement Damage in Irradiated Metals and Semiconductors*, Solid State Physics **51**, 281 (1998).

[35] W. H. Zhou, Y. G. Li, L. F. Huang, Z. Zeng, and X. Ju, *Dynamical behaviors of self-interstitial atoms in tungsten*, Journal of Nuclear Materials **437**, 438 (2013).

[36] A. L. Bement, *Irradiation effects on structural alloys for nuclear reactor applications* (ASTM International, USA, 1971), Vol. 484.

[37] T. Suzudo, M. Yamaguchi, and A. Hasegawa, *Stability and mobility of rhenium and osmium in tungsten: first principles study*, Modelling Simul. Mater. Sci. Eng. **22**, 075006 (2014).

[38] D. Kato, H. Iwakiri, Y. Watanabe, K. Morishita, and T. Muroga, *Super-saturated hydrogen effects on radiation damages in tungsten under the high-flux divertor plasma irradiation*, Nuclear Fusion **55**, 083019 (2015).

[39] M. Baldwin and R. Doerner, *Helium induced nanoscopic morphology on tungsten under fusion relevant plasma conditions*, Nuclear Fusion **48**, 035001 (2008).

[40] S. Kajita, W. Sakaguchi, N. Ohno, N. Yoshida, and T. Saeki, *Formation process of tungsten nanostructure by the exposure to helium plasma under fusion relevant plasma conditions*, Nuclear Fusion **49**, 095005 (2009).

[41] H. Iwakiri, K. Yasunaga, K. Morishita, and N. Yoshida, *Microstructure evolution in tungsten during low-energy helium ion irradiation*, Journal of Nuclear Materials **283–287, Part 2**, 1134 (2000), 9th Int. Conf. on Fusion Reactor Materials.

[42] S. Takamura, N. Ohno, D. Nishijima, and S. Kajita, *Formation of Nanostructured Tungsten with Arborescent Shape due to Helium Plasma Irradiation*, Plasma and Fusion Research **1**, 051 (2006).

[43] M. Aguirre, A. Martín, J. Pastor, J. LLorca, M. Monge, and R. Pareja, *Mechanical properties of tungsten alloys with Y_2O_3 and titanium additions*, Journal of Nuclear Materials **417**, 516 (2011).

[44] A. Giannattasio and S. G. Roberts, *Strain-rate dependence of the brittle-to-ductile transition temperature in tungsten*, Philosophical Magazine **87**, 2589 (2007).

[45] W. D. Klopp, *A review of chromium, molybdenum, and tungsten alloys*, Journal of the Less Common Metals **42**, 261 (1975).

[46] P. Hohenberg and W. Kohn, *Inhomogeneous electron gas*, Physical Review **136**, .

[47] W. Kohn and L. J. Sham, *Self-consistent equations including exchange and correlation effects*, Physical Review **140**, A1133 (1965).

[48] J. P. Perdew, K. Burke, and M. Ernzerhof, *Generalized Gradient Approximation Made Simple*, Physical Review Letters **77**, 3865 (1996), erratum, *ibid.* **78**, 1396(E) (1997).

[49] K. Burke, *Perspective on density functional theory*, The Journal of chemical physics **136**, 150901 (2012).

[50] J. P. Perdew, A. Ruzsinszky, G. I. Csonka, O. A. Vydrov, G. E. Scuseria, L. A. Constantin, X. Zhou, and K. Burke, *Restoring the density-gradient expansion for exchange in solids and surfaces*, Physical Review Letters **100**, 136406 (2008).

[51] R. Armiento and A. E. Mattsson, *Functional designed to include surface effects in self-consistent density functional theory*, Physical Review B **72**, 085108 (2005).

[52] M. Dion, H. Rydberg, E. Schröder, D. C. Langreth, and B. I. Lundqvist, *Van der Waals density functional for general geometries*, Physical review letters **92**, 246401 (2004).

[53] K. Berland and P. Hyldgaard, *Exchange functional that tests the robustness of the plasmon description of the van der Waals density functional*, Physical Review B **89**, 035412 (2014).

[54] C. Kittel and P. McEuen, *Introduction to solid state physics* (Wiley New York, ADDRESS, 1976), Vol. 8.

[55] D. Hamann, M. Schlüter, and C. Chiang, *Norm-conserving pseudopotentials*, Physical Review Letters **43**, 1494 (1979).

[56] D. Vanderbilt, *Soft self-consistent pseudopotentials in a generalized eigenvalue formalism*, Physical Review B **41**, 7892 (1990).

[57] P. E. Blöchl, *Projector augmented-wave method*, Physical Review B **50**, 17953 (1994).

[58] X.-S. Kong, X. Wu, Y.-W. You, C. S. Liu, Q. F. Fang, J.-L. Chen, G. N. Luo, and Z. Wang, *First-principles calculations of transition metal-solute interactions with point defects in tungsten*, Acta Materialia **66**, 172 (2014).

[59] L. Ventelon, F. Willaime, C.-C. Fu, M. Heran, and I. Ginoux, *Ab initio investigation of radiation defects in tungsten: Structure of self-interstitials and specificity of di-vacancies compared to other bcc transition metals*, Journal of Nuclear Materials **425**, 16 (2012).

[60] P. Erhart and K. Albe, *Thermodynamics of mono- and di-vacancies in barium titanate*, **102**, 084111 (2007).

[61] C. S. Becquart and C. Domain, *Molecular dynamics simulations of damage and plasticity: The role of ab initio calculations in the development of interatomic potentials*, **89**, 3215 (2009).

[62] M. Z. Hossain and J. Marian, *Stress-dependent solute energetics in W?Re alloys from first-principles calculations*, Acta Materialia **80**, 107 (2014).

[63] S. A. Centoni, B. Sadigh, G. H. Gilmer, T. J. Lenosky, T. Diaz de la Rubia, and C. B. Musgrave, *First-principles calculation of intrinsic defect formation volumes in silicon*, Physical Review B **72**, 195206 (2005).

[64] E. Jedvik, A. Lindman, M. Þ. Benediktsson, and G. Wahnström, *Size and shape of oxygen vacancies and protons in acceptor-doped barium zirconate*, Solid State Ionics **275**, 2 (2015).

[65] A. R. Allnatt and A. B. Lidiard, *Atomic Transport in Solids* (Cambridge University Press, Cambridge, 2003).

[66] H. Jónsson, G. Mills, and K. W. Jacobsen, in *Classical and Quantum Dynamics in Condensed Phase Simulations*, edited by B. J. Berne, G. Ciccotti, and D. F. Coker (World Scientific, Singapore, 1998), pp. 385–404.

[67] G. Henkelman and H. Jónsson, *Improved tangent estimate in the nudged elastic band method for finding minimum energy paths and saddle points*, **113**, 9978 (2000).

[68] G. Henkelman, B. P. Uberuaga, and H. Jónsson, *A climbing image nudged elastic band method for finding saddle points and minimum energy paths*, The Journal of Chemical Physics **113**, 9901 (2000).

[69] A. van de Walle, *Multicomponent multisublattice alloys, nonconfigurational entropy and other additions to the Alloy Theoretic Automated Toolkit*, Calphad **33**, 266 (2009).

[70] A. van de Walle, *Methods for first-principles alloy thermodynamics*, JOM **65**, 1523 (2013).

[71] L. J. Nelson, V. Ozoliņš, C. S. Reese, F. Zhou, and G. L. Hart, *Cluster expansion made easy with Bayesian compressive sensing*, Physical Review B **88**, 155105 (2013).

[72] J. M. Sanchez, F. Ducastelle, and D. Gratias, *Generalized cluster description of multicomponent systems*, Physica **128**, 334 (1984).

[73] L. J. Nelson, G. L. Hart, F. Zhou, V. Ozoliņš, *et al.*, *Compressive sensing as a paradigm for building physics models*, Physical Review B **87**, 035125 (2013).

[74] E. Candes and M. Wakin, *An Introduction To Compressive Sampling*, Signal Processing Magazine, IEEE **25**, 21 (2008).

[75] B. Sadigh and P. Erhart, *Calculations of excess free energies of precipitates via direct thermodynamic integration across phase boundaries*, Phys. Rev. B **86**, 134204 (2012).

[76] *Property change mechanism in tungsten under neutron irradiation in various reactors*, Journal of Nuclear Materials **417**, 491 (2011), proceedings of ICFRM-14.

[77] T. Tanno, A. Hasegawa, J.-C. He, M. Fujiwara, S. Nogami, M. Satou, T. Shishido, and K. Abe, *Effects of Transmutation Elements on Neutron Irradiation Hardening of Tungsten*, MATERIALS TRANSACTIONS **48**, 2399 (2007).

[78] L. Gharaee and P. Erhart, *A first-principles investigation of interstitial defects in dilute tungsten alloys*, Journal of Nuclear Materials **467**, 448 (2015).

[79] L. Gharaee, J. Marian, and P. Erhart, *The role of interstitial binding in radiation induced segregation in W-Re alloys*, Journal of Applied Physics **120**, 025901 (2016).

[80] C. H. Huang, L. Gharaee, Y. Zhao, P. Erhart, and J. Marian, *Mechanism of Re precipitation in irradiated W-Re alloys from kinetic Monte Carlo simulations*, arXiv preprint arXiv:1702.03019 , (2017).

[81] L. Gharaee, P. Erhart, and P. Hyldgaard, *Finite-temperature properties of non-magnetic transition metals: Comparison of the performance of constraint-based semi and nonlocal functionals*, Physical Review B **95**, 085147 (2017).

[82] L. Gharaee, M. Ångqvist, M. Rahm, and P. Erhart, *Structurally driven asymmetric miscibility in the phase diagram of W-Ti*, In manuscript , (2017).

[83] E. Rudy and S. Windisch, *Revision of titanium-tungsten system*, Trans. Metall. Soc. AIME **242**, 953 (1968).

[84] J. L. Murray, *The Ti-W (Titanium-Tungsten) System*, Bull. Alloy Phase Diagrams **2**, 192 (1981).

[85] L. Kaufman and H. Nesor, *Calculation of Superalloy Phase Diagrams: Part IV*, Metall. Trans. **6A**, 2123 (1975).

[86] S. K. Lee and D. N. Lee, *CALCULATION OF PHASE DIAGRAMS USING PARTIAL PHASE DIAGRAM DATA*, Calphad **10**, 61 (1986).

[87] S. Jönsson, *Reevaluation of the Ti-W system and prediction of the Ti-W-N phase diagram*, Zeitschr. Metallkunde **87**, 784 (1996).

[88] P. Olsson, I. A. Abrikosov, and J. Wallenius, *Electronic origin of the anomalous stability of Fe-rich bcc Fe-Cr alloys*, Physical Review B **73**, 104416 (2006).

[89] T. P. C. Klaver, R. Drautz, and M. W. Finnis, *Magnetism and thermodynamics of defect-free Fe-Cr alloys*, Phys. Rev. B **74**, 094435 (2006).

[90] G. J. Ackland, *Magnetically Induced Immiscibility in the Ising Model of FeCr Stainless Steel*, Physical Review Letters **97**, 015502 (2006).

[91] A. T. Dinsdale, *SGTE data for pure elements*, CALPHAD **15**, 317 (1991).

[92] A. Litnovsky, T. Wegener, F. Klein, C. Linsmeier, M. Rasinski, A. Kreter, B. Unterberg, M. Vogel, S. Kraus, U. Breuer, C. Garcia-Rosales, A. Calvo, and N. Ordas, *Smart alloys for a future fusion power plant: First studies under stationary plasma load and in accidental conditions*, Nuclear Materials and Energy , (2016).